Front. Earth Sci. 2025, 19(2): 168–187
https://doi.org/10.1007/s11707-024-1123-0

RESEARCH ARTICLE

Geochemical characteristics of the late Eocene mudstones in the eastern Nima Basin, Xizang: implications for the paleoenvironment, provenance, and tectonic setting

Xinhang WANG[1], Siqi XIAO[2], Zhongpeng HAN (✉)[3,4], Yalin LI[1,3], Shuai LI[1], Jie DAI[5]

1 School of Earth Sciences and Resources, China University of Geosciences (Beijing), Beijing 100083, China
2 Yunnan Provincial Energy Investment Group Co., ltd, Kunming 650228, China
3 Frontiers Science Center for Deep-time Digital Earth, China University of Geosciences (Beijing), Beijing 100083, China
4 Institute of Earth Sciences, China University of Geosciences (Beijing), Beijing 100083, China
5 Key Laboratory of Sedimentary Basin and Oil and Gas Resources (Ministry of Natural Resources), Chengdu 610081, China

Abstract Paleoenvironmental reconstruction plays a pivotal role in providing insights into the uplift history of the Xizang Plateau during the Cenozoic. The Nima Basin, situated in the central Xizang Plateau, is crucial for studying the tectonic and geomorphic evolution of this region. The clastic composition and geochemical characteristics of the Niubao Formation hold considerable potential for unravelling the geological history and reconstructing depositional environments of central Xizang in the early Cenozoic. In this study, we present detailed geochemical characteristics to determine their provenance, paleoenvironmental conditions, and tectonic origins. The index of compositional variability (ICV > 1) of mudstones indicates that low compositional maturity sediments underwent weak sedimentary recycling. The chemical index of alteration (CIA: 59.8–72.9) reveals that parental rocks experienced a moderate chemical weathering degree. The paleoclimate indicators of the mudstones suggest an oxidizing and arid depositional environment, with a mean annual temperature (MAT) of 11.64°C ± 4.19°C. The geochemical evidence also demonstrates that the mudstones were derived from mixed felsic and intermediate igneous rocks that formed in a dominantly continental island arc tectonic setting. Similarities in the geochemical characteristics among the Niubao Formation and surrounding igneous rocks indicate that a continental-scale drainage system once drained westward in central Xizang. It is concluded that the central plateau experienced a cooler and drier climate coinciding with the presence of a large-scale drainage system during the late Eocene.

Received October 16, 2023; accepted March 6, 2024

E-mail: hanzp@cugb.edu.cn

Keywords late Eocene, geochemistry, Nima Basin, mudstone, paleoenvironment

1 Introduction

The early Cenozoic continental collision between the India and Asia accelerated the outward growth of the Xizang Plateau from central Xizang and significantly influenced the Cenozoic global climate and the development of the Asian monsoon system (Raymo and Ruddiman, 1992; Molnar et al., 1993, 2010; Cerling et al., 1997; Dupont-Nivet et al., 2007; Ding et al., 2014; Deng and Ding, 2015; Kapp and DeCelles, 2019; Ingalls et al., 2020; Yang et al., 2022; Feng et al., 2023). Nonetheless, the comprehension of the Cenozoic geomorphological and paleoenvironmental evolution in central Xizang remains a subject of intense debate, primarily due to methodological disparities among studies (Wang et al., 2014a; Su et al., 2019; Spicer et al., 2021a, 2021b; Ding et al., 2022). Several Cenozoic intermountain basins, developed in the Bangong-Nujiang Suture Zone (BNSZ) in central Xizang, accumulated up to 4 km of fluvio-lacustrine sediments that contain crucial paleogeographic evolution records. The isotopic compositions of carbonates obtained from those basins suggest arid and cold conditions during the Paleogene (Rowley and Currie, 2006; DeCelles et al., 2007b), whereas the same successions have yielded fossils of mammals (Deng et al., 2012), fish (Wu et al., 2017), plants (Jia et al., 2019; Jiang et al., 2019; Liu et al., 2019; Su et al., 2019; Tang et al., 2019), and biomarker remains (Jia et al., 2015) that reflect a warm and humid environment. The stable isotope analyses of paleosol carbonate in the Nima Basin

point to an arid climate and high paleoelevation (4.5–5 km) by 26 Ma (Rowley and Currie, 2006; DeCelles et al., 2007a; Sun et al., 2014; Ingalls et al., 2020), whereas the paleontological evidence provided by the ecological signal of plant megafossils and fish suggests that tropical-subtropical warm and humid lowland habitats were present in the Xizang interior ca. 26 Ma, probably at an elevation of ~1 km (Wu et al., 2017). Additionally, reliable chronological frameworks (Han et al., 2019; Fang et al., 2020; Xiong et al., 2022) and numerical simulation models (Botsyun et al., 2019; Su et al., 2020) have resolved the disparities between paleontological and isotopic geochemistry investigations.

During the process of weathering, erosion, transport, deposition, and diagenesis, geochemical elements in source rocks exhibit stable chemical characteristics, resulting in minimal differentiation in fine-grained sediments (Nesbitt, 1979; Nesbitt and Markovics, 1997; Duddy, 1980; Bhatia, 1983; McLennan et al., 1983; Taylor and McLennan, 1985; Wronkiewicz and Condie, 1987; Crichton and Condie, 1993; Vital and Stattegger, 2000; Weltje and von Eynatten, 2004; Singh, 2009; Moradi et al., 2016; Caracciolo, 2020; Wang et al., 2020; Amorosi et al., 2022). The geochemistry of clastic sediments is an essential source of information for determining their provenance history (Girty et al., 1993; Cullers and Podkovyrov, 2000; Anderson et al., 2002; Wang et al., 2018a; Ramos-Vázquez and Armstrong-Altrin, 2019; Chen et al., 2020; Banerji et al., 2022), as well as their tectonic background (Roy et al., 2008; Gallala et al., 2009; Armitage et al., 2011; Bai et al., 2015; Wang et al., 2017a; Wang et al., 2018a; Lin et al., 2021; Sun et al., 2022).

The Paleocene to Eocene Niubao Formation is extensively distributed within the Bangong-Nujiang Suture Zone (BNSZ) and is one of the predominant Cenozoic strata in central Xizang. Although numerous paleontological identifications and hydrocarbon explorations have been conducted on the Niubao Formation, further geochemical studies are required to gain a comprehensive understanding of the paleoenvironment of the Niubao Formation. In this study, the geochemical characteristics of mudstones were analyzed in the Niubao Formation in the Nima Basin, with a comparative examination against neighboring igneous rocks. Additionally, the study applies an empirical formula to calculate the mean annual temperature (MAT) of the source area. The primary objective is to elucidate the origin and tectonic setting of the Niubao Formation and to provide a new perspective on the early Cenozoic paleogeomorphic pattern of central Xizang.

2 Geological background

The Qiangtang and Lhasa terranes are divided by the Bangong-Nujiang Suture Zone, which extends approximately 2000 km from east to west in central Xizang. The Nima Basin, one of the largest Cenozoic sedimentary basins within the BNSZ, spans an east–west-trending region with an area of 3000 km^2 (Fig. 1; DeCelles et al., 2007a, 2007b; Kapp et al., 2007; Chen et al., 2022). The Cenozoic terrestrial strata in the Nima Basin unconformably overlie deformed Mesozoic marine strata. The margins of the basin are strongly deformed by east–west basin-controlling faults along the northern and southern margins. Previous research has revealed that the Niubao Formation was deposited predominantly in a fluvial to deltaic environment during the Paleocene to Eocene. The Niubao Formation is distinguished by red upward-fining or upward-coarsening sequences of conglomerate, sandstone, siltstone, and mudstone, with occasional thin interlayers of marl and limestone that likely represent lacustrine facies. Recent investigations constructed a chronostratigraphic framework for the Niubao Formation using the ages of volcaniclastic interlayers as chronological anchors. Tuffaceous and paleomagnetic stratigraphic results in the Lunpola basin yielded an age range of 41.8–21.5 Ma for the middle to the upper part of the Niubao Formation (Fang et al., 2020). Su et al. (2020) obtained a zircon U-Pb age of 47.5 ± 0.7 Ma from a tephra-rich layer in the Niubao Formation in the Bangoin Basin. Xiong et al. (2022) established a depositional age range of 50–29 Ma for the Niubao Formation, extending from the base to the top of the formation.

In this study, a 410-m-thick stratigraphic section of the Niubao Formation was measured in the field on the south-eastern margin of the Nima Basin (31°57′04.30″N, 88°24′42.87″E; Fig. 2). The sedimentary profile is dominated by red and grayish-green mudstones with a total thickness of approximately 200 m. The interbedded conglomerates, sandstones, and siltstones are characterized by kinds of sedimentary structure, including parallel or horizontal bedding, cross-bedding, and bioturbation. This section is near the Kanggale section (31°58′21.38″N, 88°26′10.19″E), where notable late Eocene fossils of Spittlebugs and Lestidae were discovered (Xia et al., 2022; Xu et al., 2022). The fossiliferous strata in Kanggale consist of similar grayish-green mudstones and calcareous shales, with interbedded mudstones, sandstones, and limestones within these layers (Xia et al., 2022). The striking similarity in lithologic composition and sedimentary features between the studied section and the Kanggale section indicates that the depositional age of the measured section in this study is assigned to the late Eocene.

3 Sampling and analytical methods

3.1 Sampling

Eighteen mudstone samples were systemically collected

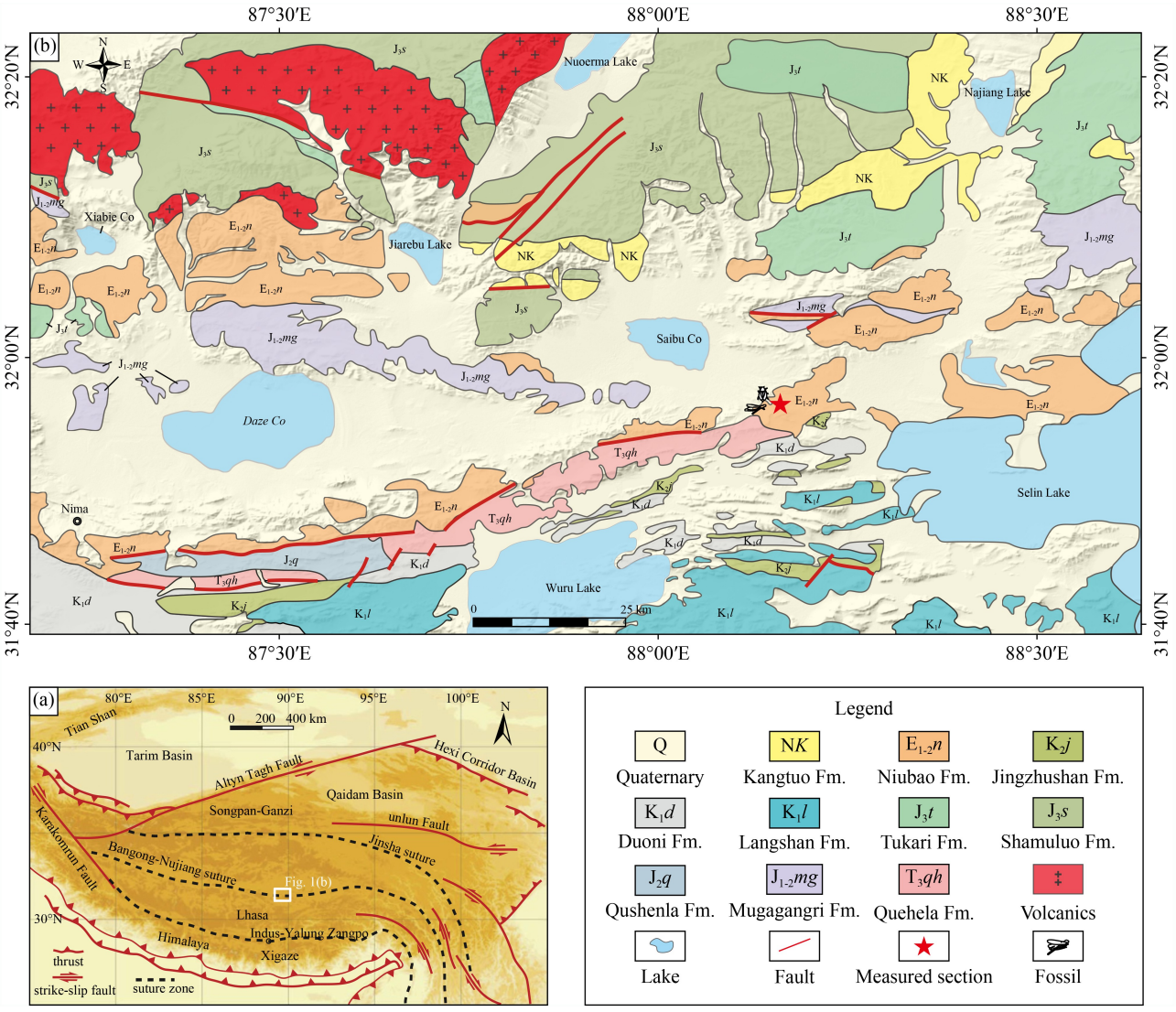

Fig. 1 (a) Primary terranes of the Xizang Plateau (modified from Li et al., 2015). (b) Geological map of the Nima Basin (modified from Chen et al., 2020).

from different stratigraphic intervals for geochemical analysis. The sampling locations are shown in Fig. 2. To minimize weathering effects, we selected unweathered samples and carefully removed weathering surfaces. All the samples were crushed in the laboratory before analysis.

3.2 Analytical methods

Major element, trace element, and rare earth element (REE) analyses were completed at Wuhan Sample Solution Analytical Technology Co., Ltd., Wuhan, China. Whole-rock major oxide concentrations were measured using an X-ray fluorescence spectrometer (XRF). The whole-rock major element analysis samples were prepared by the fusion bead method. For this procedure, samples were collected and pulverized to a size of less than 200 mesh using an agate mortar. Approximately 1 g of fine powdered sample was then fused with a 6 g flux, consisting of a well-balanced mixture of lithium tetraborate, lithium metaborate, and lithium fluoride at a ratio of 45:10:5, to form a uniform glass bead. Ammonium nitrate and lithium bromide were used as oxidant and release agents, respectively. The melting temperature was 1050°C and was maintained for 15 min. Measurements were made using a ZSX Primus II wavelength dispersive XRF instrument (RIGAKU, Japan) with a 4.0 kW Rh target X-ray tube at 50 kV and 60 mA. Quality control was ensured using physical and analysis replicates and the reference material GBW07101-14. The data were corrected by the theoretical α coefficient method, and the relative standard deviation (RSD) was less than 2%.

Whole-rock trace element analysis and REE analysis were conducted on an Agilent 7700e ICP-MS instrument. In the pretreatment phase for geochemical trace and REE

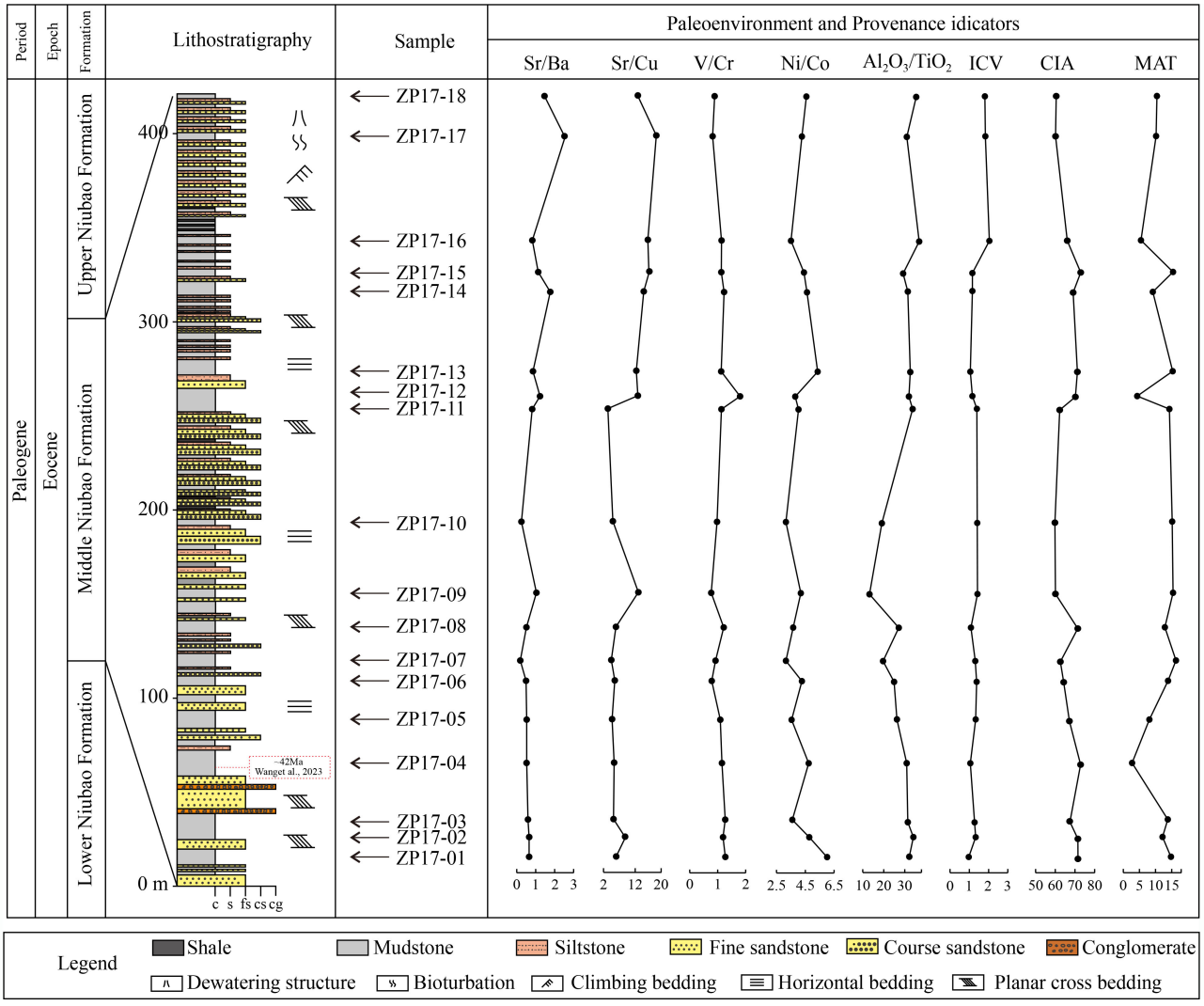

Fig. 2 The stratigraphic chart of the studied section and line chart depicting changes in paleoenvironmental and provenance indicators. The age of the section is determined through stratigraphic correlation (Xia et al., 2022; Wang et al., 2023).

analysis, the sample powder, with a 200 mesh size, was initially dried for 12 h at 105°C. A 50 mg portion of this powder was then accurately weighed and placed in a Teflon bomb, to which 1 mL of HNO_3 and 1 mL of HF were added. This mixture was heated in a stainless steel jacket at 190°C for more than 24 h and then cooled. The contents were evaporated to near dryness, treated with HNO_3, and evaporated again. A mixture of HNO_3, Milli-Q water, and 1 mL of internal standard solution with 1 ppm In was added, and the Teflon bomb was resealed and placed in the oven for more than 12 h. The final solution was transferred to a polyethylene bottle and diluted with 2% HNO_3 to a total of 100 g.

The analysis employed a GeolasPro laser ablation system integrated with a COMPexPro 102 ArF excimer laser, featuring a 193 nm wavelength and 200 mJ maximum energy, alongside a MicroLas optical system. Trace element compositions were determined using an Agilent 7700e ICP-MS instrument, with helium as the carrier gas and argon as the makeup gas, which was fed into the ICP through a T-connector. This system includes a "wire" signal smoothing device (Hu et al., 2015). The laser parameters were set to a 40 μm spot size and a 10 Hz frequency. Calibration was conducted using the reference materials NIST 610 and NIST 612. Each sample underwent a 20−30 s background acquisition followed by a 50 s data acquisition from the sample. The off-line selection, integration of the background and analytical signals, time-drift correction, and quantitative calibration were performed using the ICPMS DataCal 10.1 software (Lin et al., 2016).

4 Results

A total of 18 representative samples of the studied section were analyzed for major, trace, and rare earth elements. The results are given in Tables 1, 2, and 3.

Table 1 Composition of major elements, ICV, CIA, and MAT values in the mudstones of the Niubao Formation in the study area

Sample	ZP-01	ZP-02	ZP-03	ZP-04	ZP-05	ZP-06	ZP-07	ZP-08	ZP-09	ZP-10	ZP-11	ZP-12	ZP-13	ZP-14	ZP-15	ZP-16	ZP-17	ZP-18
SiO_2	54.50	47.05	50.70	53.24	58.57	64.45	67.82	60.70	73.10	63.42	50.07	41.12	54.86	50.89	54.01	37.23	52.60	51.01
TiO_2	0.69	0.66	0.69	0.72	0.68	0.78	0.61	0.73	0.52	0.64	0.76	0.44	0.76	0.65	0.69	0.53	0.58	0.60
Al_2O_3	19.33	17.27	17.04	19.70	14.68	12.34	10.02	16.43	8.57	12.10	17.91	14.57	17.75	19.16	16.84	12.80	7.83	9.50
TFe_2O_3	5.15	6.27	6.17	5.46	5.48	3.67	3.37	5.86	3.76	5.07	6.50	4.40	6.90	6.08	5.69	4.99	3.14	3.76
MnO	0.04	0.07	0.12	0.07	0.12	0.11	0.15	0.06	0.08	0.11	0.09	0.11	0.06	0.05	0.07	0.16	0.12	0.11
MgO	2.69	4.36	3.37	3.51	3.16	2.65	1.54	2.59	1.32	1.91	3.48	2.86	2.38	3.49	3.44	6.16	2.51	3.08
CaO	3.63	7.38	6.96	4.08	5.05	5.36	6.47	3.01	4.83	5.83	5.72	15.47	3.92	3.48	5.36	14.17	15.05	13.33
Na_2O	1.04	0.81	1.32	0.95	1.25	1.40	1.28	1.01	1.38	1.82	2.19	0.89	0.87	1.34	0.85	0.95	1.13	1.25
K_2O	3.96	3.98	3.63	3.88	2.83	2.08	1.64	2.98	1.09	1.98	3.40	3.02	3.99	3.86	3.20	3.18	1.36	1.96
P_2O_5	0.15	0.13	0.17	0.15	0.15	0.16	0.11	0.10	0.08	0.12	0.15	0.11	0.13	0.12	0.09	0.14	0.12	0.12
LOI	8.74	11.33	9.82	7.91	8.10	7.38	7.36	6.56	5.70	7.28	9.41	16.36	8.13	10.23	9.86	19.26	15.74	14.61
Total	91.18	87.97	90.18	91.75	91.95	93.00	93.00	93.47	94.72	92.99	90.26	82.98	91.63	89.11	90.24	80.31	84.44	84.70
ICV	0.97	1.33	1.27	1.05	1.33	1.38	1.28	1.08	1.42	1.41	1.39	1.16	1.05	1.16	1.16	2.04	1.83	1.81
CIA	71.49	71.16	67.30	72.83	67.16	64.21	62.58	71.44	60.04	59.79	62.20	70.21	71.17	69.03	72.90	66.04	60.13	60.44
MAT	14.79	11.99	13.79	2.71	8.11	13.89	16.35	12.91	15.44	15.17	14.30	4.32	15.33	9.14	15.42	5.50	10.18	10.44

Table 2 Trace element concentration in mudstones of the Niubao Formation (unit in ppm)

Sample	ZP-01	ZP-02	ZP-03	ZP-04	ZP-05	ZP-06	ZP-07	ZP-08	ZP-09	ZP-10	ZP-11	ZP-12	ZP-13	ZP-14	ZP-15	ZP-16	ZP-17	ZP-18
Sc	17.0	16.4	15.9	17.2	13.5	11.6	8.8	14.5	7.2	10.6	17.8	12.2	16.3	16.4	15.3	11.8	8.1	10.1
V	123	131	140	121	95	83	63	100	51	71	120	114	114	121	104	90	58	72
Cr	97	112	110	105	87	106	68	83	66	73	106	63	102	98	92	79	71	80
Co	11.1	16.9	17.0	13.2	14.9	13.5	10.2	13.4	7.2	12.3	17.8	12.0	14.0	15.0	14.2	14.3	9.5	12.2
Ni	67	80	61	62	53	58	32	49	30	39	72	46	75	69	62	50	41	56
Cu	31	34	29	27	27	19	31	25	14	30	62	25	21	29	25	24	18	19
Zn	100	90	84	109	84	78	57	93	59	70	85	77	95	84	87	68	43	55
Ga	23.6	23.3	22.2	25.6	19.4	15.5	12.1	21.4	10.4	14.6	22.7	19.1	23.1	25.0	21.6	16.7	9.5	12.1
Y	32.3	25.9	25.4	30.7	30.6	27.4	29.7	31.3	23.7	30.0	24.5	23.3	31.5	27.4	30.4	20.4	22.6	23.1
Zr	141	131	146	153	167	200	203	172	249	217	150	100	153	138	156	107	132	120
Nb	14.6	14.1	13.0	15.3	14.4	15.3	13.2	15.6	11.3	14.5	12.9	9.6	16.5	14.1	14.9	10.5	11.5	12.0
Hf	3.89	3.56	3.82	4.08	4.39	5.22	5.27	4.63	6.37	5.65	4.18	2.95	4.26	3.79	4.30	2.98	3.43	3.23
Ta	1.08	0.99	0.92	1.15	1.08	1.06	0.97	1.15	0.84	1.09	1.03	0.81	1.26	1.08	1.13	0.81	0.85	0.88
Th	20.27	14.93	13.56	18.51	15.69	12.31	12.43	17.76	11.35	15.89	12.84	16.65	18.51	17.30	18.03	11.80	9.54	10.99
U	6.77	5.71	4.04	4.89	3.54	3.24	2.63	3.61	2.74	3.21	2.16	5.49	2.78	4.15	3.22	2.27	2.04	2.23
Rb	194.48	177.27	170.51	193.46	143.62	100.97	85.58	154.31	57.91	107.34	156.25	155.66	196.24	192.18	166.07	137.51	64.39	90.66
Sr	188	293	152	144	129	108	140	150	180	150	210	322	260	432	408	387	329	244
Cs	22.39	19.19	13.91	15.21	13.07	5.96	8.09	15.05	4.49	11.16	19.09	16.37	20.88	22.51	17.22	15.79	5.72	8.01
Ba	289	467	255	277	244	219	739	290	173	601	256	261	304	244	360	468	131	166
Pb	32.6	23.7	29.4	20.0	30.3	12.0	18.3	25.7	19.1	34.9	22.1	27.3	24.7	27.5	28.4	22.1	18.4	19.8

4.1 Major elements

Major element analyses were carried out on 18 mudstone samples of the Niubao Formation of the Nima Basin, as detailed in Table 1. The total content of major components in the mudstone ranges from 80.31 to 94.72 wt.%. The results revealed that SiO_2, Al_2O_3, CaO, and Fe_2O_3 were the predominant components, followed closely by MgO and K_2O. The concentrations of other components, such as TiO_2, P_2O_5, and MnO, were generally less than 1.0%.

The mudstone samples exhibited noticeable variations

Table 3 REE contents in mudstones of the Niubao Formation (unit in ppm)

Sample	ZP-01	ZP-02	ZP-03	ZP-04	ZP-05	ZP-06	ZP-07	ZP-08	ZP-09	ZP-10	ZP-11	ZP-12	ZP-13	ZP-14	ZP-15	ZP-16	ZP-17	ZP-18
Sc	17.0	16.4	15.9	17.2	13.5	11.6	8.8	14.5	7.2	10.6	17.8	12.2	16.3	16.4	15.3	11.8	8.1	10.1
V	123	131	140	121	95	83	63	100	51	71	120	114	114	121	104	90	58	72
Cr	97	112	110	105	87	106	68	83	66	73	106	63	102	98	92	79	71	80
Co	11.1	16.9	17.0	13.2	14.9	13.5	10.2	13.4	7.2	12.3	17.8	12.0	14.0	15.0	14.2	14.3	9.5	12.2
Ni	67	80	61	62	53	58	32	49	30	39	72	46	75	69	62	50	41	56
Cu	31	34	29	27	27	19	31	25	14	30	62	25	21	29	25	24	18	19
Zn	100	90	84	109	84	78	57	93	59	70	85	77	95	84	87	68	43	55
Ga	23.6	23.3	22.2	25.6	19.4	15.5	12.1	21.4	10.4	14.6	22.7	19.1	23.1	25.0	21.6	16.7	9.5	12.1
Y	32.3	25.9	25.4	30.7	30.6	27.4	29.7	31.3	23.7	30.0	24.5	23.3	31.5	27.4	30.4	20.4	22.6	23.1
Zr	141	131	146	153	167	200	203	172	249	217	150	100	153	138	156	107	132	120
Nb	14.6	14.1	13.0	15.3	14.4	15.3	13.2	15.6	11.3	14.5	12.9	9.6	16.5	14.1	14.9	10.5	11.5	12.0
Hf	3.89	3.56	3.82	4.08	4.39	5.22	5.27	4.63	6.37	5.65	4.18	2.95	4.26	3.79	4.30	2.98	3.43	3.23
Ta	1.08	0.99	0.92	1.15	1.08	1.06	0.97	1.15	0.84	1.09	1.03	0.81	1.26	1.08	1.13	0.81	0.85	0.88
Th	20.27	14.93	13.56	18.51	15.69	12.31	12.43	17.76	11.35	15.89	12.84	16.65	18.51	17.30	18.03	11.80	9.54	10.99
U	6.77	5.71	4.04	4.89	3.54	3.24	2.63	3.61	2.74	3.21	2.16	5.49	2.78	4.15	3.22	2.27	2.04	2.23
Rb	194.48	177.27	170.51	193.46	143.62	100.97	85.58	154.31	57.91	107.34	156.25	155.66	196.24	192.18	166.07	137.51	64.39	90.66
Sr	188	293	152	144	129	108	140	150	180	150	210	322	260	432	408	387	329	244
Cs	22.39	19.19	13.91	15.21	13.07	5.96	8.09	15.05	4.49	11.16	19.09	16.37	20.88	22.51	17.22	15.79	5.72	8.01
Ba	289	467	255	277	244	219	739	290	173	601	256	261	304	244	360	468	131	166
Pb	32.6	23.7	29.4	20.0	30.3	12.0	18.3	25.7	19.1	34.9	22.1	27.3	24.7	27.5	28.4	22.1	18.4	19.8

in their elemental compositions. The SiO_2 content varied widely, from 37.23 to 73.10 wt.%, averaging 54.74 wt.%. Al_2O_3 ranged from 7.83 to 19.70 wt.%, with a mean of 14.66 wt.%. The content of total Fe_2O_3 ranges from 3.14 to 6.90 wt.%, averaging at 5.10 wt.%. The TiO_2 content varies between 0.44 and 0.78 wt.%, with a mean value of 0.65 wt.%. The CaO content spaned from 3.01 to 15.47 wt.%, averaging at 7.17 wt.%. The K_2O content is 1.09−3.99 wt.% with an average of 2.89 wt.%. The Na_2O content is in the range of 0.81−2.19 wt.% with an average of 1.21 wt.%. Additionally, the loss on ignition (LOI) ranged from 5.70 to 19.26 wt.%, potentially attributable to organic matter or volatile components.

The ratios of the concentrations of the major elements in the mudstones to those in the upper continental crust (UCC) are shown in Fig. 3(a). In addition to some samples being enriched in CaO and K_2O, all the samples exhibited apparent depletion in Na_2O, with the remaining element concentrations plotting near those in the UCC.

4.2 Trace and REEs

The trace element data of the mudstone samples are listed in Table 2 and have been standardized in relation to the average UCC values (Taylor and McLennan, 1985; Fig. 3(b)). The trace element analyses reveal that, compared with the UCC, the mudstone samples are significantly enriched in Ni, Zn, Rb, Cs, Th, and U and depleted in Co, Sr, Ba, Zr, and Hf.

The REE analysis results are presented in Table 3 and data are plotted in the chondrite-normalized diagram (Fig. 3(c)). The mudstones have total REE (ΣREE) ranging from 124.81 to 204.83 ppm, with an average of 162.34 ppm. the average value is slightly lower than the post-Archean Australian shale (PAAS) value of 211.76 ppm (Taylor and McLennan, 1985; McLennan et al., 2006). In terms of chondrite-normalized REE patterns, the mudstones closely align with PAAS. Light REEs (LREEs) in mudstones range from 109.76 to 183.43 ppm, while heavy REEs (HREEs) range from 13.86 to 21.40 ppm. Generally, the mudstones exhibit higher concentrations of LREEs than HREEs. The ratios of LREEs to HREEs in these samples vary from 7.29 to 9.24, with an overall average of 8.29, indicating relative enrichment of LREEs in the mudstones. Additionally, the mudstones exhibit consistent negative Eu anomalies, with values ranging from 0.59 to 0.70 and an average of 0.65.

4.3 Mineral composition

The high SiO_2 and low Al_2O_3 contents suggest that clay minerals are the main mineral component of the mudstone. The low Na_2O concentrations suggest the minimal presence of plagioclase in the samples (Ross and Bustin, 2009; Zeng et al., 2020). The high levels of CaO are likely attributable to the presence of carbonate

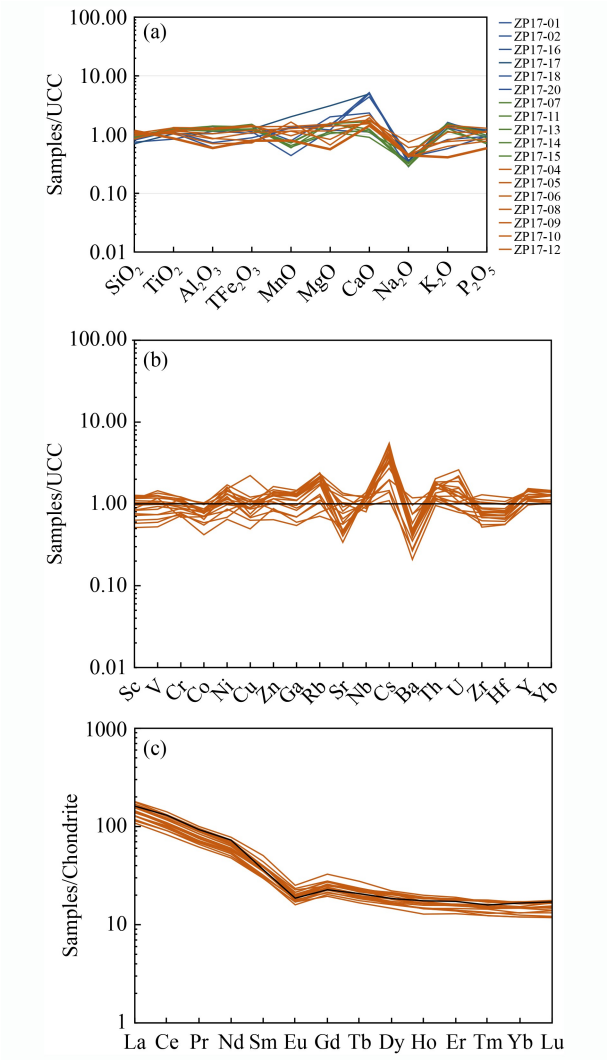

Fig. 3 (a) Upper continental crust (UCC)-normalized ratios for major elements. (b) Trace element compositions normalized against the upper continental crust (UCC) for the mudstones. (c) Chondrite-normalized rare earth elements (REEs) plot for the mudstone samples.

minerals, which are present in the formation of cement (Ghosh and Sarkar, 2010). Notably, the mudstones exhibit significant correlations between TFe_2O_3 and Al_2O_3 (R^2 = 0.847) and K_2O (R^2 = 0.865; Table 4), indicating the close association of Fe with clay minerals.

The K_2O/Al_2O_3 ratio provides valuable insight into the primary mineral constituents within sediments. A ratio between 0.2 and 0.3 generally implies the dominance of illite in the sediment. Conversely, a ratio near 0 is indicative of sediment enriched with minerals such as kaolinite, smectite, and vermiculite (Cox et al., 1995; Zhou et al., 2015; Zeng et al., 2020). The K_2O/Al_2O_3 ratios in mudstone vary from 0.13 to 0.25, averaging 0.19 (Table 5). The highest value was obtained for the ZP-16 sample (0.25), and the lowest value was obtained for the ZP-09 sample (0.13). These data indicate that the ratio aligns with typical values for clay minerals, suggesting that illite is the predominant clay mineral present. Additionally, the notable associations between Sc, V, Zn, Ga, Rb, and both Al_2O_3 and K_2O indicate that these elements are predominantly related to clay minerals (Table 4).

5 Discussion

5.1 Sediment maturity and paleoweathering

The index of compositional variability (ICV) can determine the original character and maturity of sediments. Generally, ICV value < 1 indicates that the sample is intensively mature, rich in clay minerals, and may have undergone recycling or strong weathering during the first cycle of deposition, while ICV value > 1 indicates that the sample has a low maturity and a low clay mineral content (Barshad, 1966). For the studied samples, the ICV values of all the mudstones exhibit

Table 4 Correlation matrix of major and trace elements of the mudstones (* indicates $p < 0.05$; ** indicates $p < 0.01$, both suggesting statistically significant correlations)

	Al_2O_3	SiO_2	TiO_2	TFe_2O_3	MnO	CaO	MgO	Na_2O	K_2O	P_2O_5	Sc	V	Cr	Co	Ni
Al_2O_3	1														
SiO_2	−0.618**	1													
TiO_2	0.502*	−0.089	1												
TFe_2O_3	0.847**	−0.612**	0.494*	1											
MnO	−0.516*	−0.151	−0.391	−0.374	1										
CaO	−0.382	−0.465	−0.528*	−0.315	0.692**	1									
MgO	0.390	−0.832**	0.092	0.455	0.350	0.432	1								
Na_2O	−0.216	0.206	0.116	−0.078	0.174	−0.075	−0.181	1							
K_2O	0.953**	−0.769**	0.433	0.865**	−0.347	−0.178	0.572*	−0.318	1						
P_2O_5	0.386	−0.540*	0.432	0.303	0.284	0.154	0.525*	0.105	0.488*	1					
Sc	0.968**	−0.540*	0.672**	0.860**	−0.551*	−0.462	0.332	−0.111	0.909**	0.424	1				
V	0.945**	−0.665**	0.474*	0.829**	−0.396	−0.266	0.398	−0.197	0.936**	0.506*	0.934**	1			
Cr	0.701**	−0.317	0.826**	0.645**	−0.427	−0.478*	0.292	−0.010	0.677**	0.563*	0.816**	0.754**	1		

(*continued*)

	Al_2O_3	SiO_2	TiO_2	TFe_2O_3	MnO	CaO	MgO	Na_2O	K_2O	P_2O_5	Sc	V	Cr	Co	Ni
Co	0.685**	−0.601**	0.623**	0.810**	−0.055	−0.171	0.550*	0.149	0.712**	0.544*	0.760**	0.763**	0.758**	1	
Ni	0.806**	−0.558*	0.704**	0.773**	−0.501*	−0.288	0.410	−0.142	0.833**	0.454	0.877**	0.819**	0.881**	0.756**	1
Cu	0.476*	−0.304	0.390	0.495*	−0.094	−0.226	0.168	0.579*	0.392	0.278	0.558*	0.477*	0.400	0.610**	0.414
Zn	0.900**	−0.327	0.576*	0.722**	−0.637**	−0.605**	0.159	−0.288	0.801**	0.297	0.897**	0.820**	0.695**	0.542*	0.697**
Ga	0.989**	−0.535*	0.549*	0.853**	−0.564*	−0.475*	0.322	−0.227	0.925**	0.347	0.974**	0.937**	0.737**	0.698**	0.807**
Rb	0.983**	−0.609**	0.484*	0.853**	−0.507*	−0.371	0.365	−0.327	0.963**	0.372	0.944**	0.931**	0.670**	0.649**	0.799**
Sr	0.208	−0.578*	−0.224	0.268	0.021	0.438	0.536*	−0.271	0.326	−0.159	0.098	0.144	−0.078	0.121	0.245
Nb	0.424	0.265	0.779**	0.371	−0.628**	−0.809**	−0.263	−0.159	0.296	0.017	0.530*	0.313	0.595**	0.299	0.478*
Cs	0.921**	−0.645**	0.365	0.855**	−0.480*	−0.276	0.399	−0.206	0.921**	0.247	0.870**	0.835**	0.519*	0.595**	0.760**
Ba	−0.047	0.089	−0.108	0.019	0.301	−0.102	0.025	−0.006	−0.012	−0.152	−0.085	−0.097	−0.168	0.030	−0.198
Th	0.766**	−0.199	0.301	0.557*	−0.681**	−0.542*	−0.063	−0.413	0.652**	−0.024	0.695**	0.618**	0.326	0.220	0.459
U	0.610**	−0.296	−0.015	0.272	−0.463	−0.214	0.050	−0.432	0.568*	0.204	0.512*	0.631**	0.309	0.128	0.381
Zr	−0.458	0.913**	−0.050	−0.395	−0.164	−0.589*	−0.705**	0.304	−0.624**	−0.471*	−0.394	−0.519*	−0.193	−0.420	−0.485*
Hf	−0.402	0.894**	−0.025	−0.343	−0.214	−0.625**	−0.710**	0.304	−0.578*	−0.491*	−0.341	−0.477*	−0.174	−0.392	−0.445
Yb	0.556*	0.197	0.564*	0.448	−0.635**	−0.833**	−0.322	−0.143	0.387	−0.024	0.602**	0.428	0.430	0.269	0.375
∑REE	0.766**	−0.154	0.478*	0.539*	−0.684**	−0.617**	−0.027	−0.475*	0.672**	0.121	0.745**	0.651**	0.507*	0.291	0.566*
LREE	0.786**	−0.189	0.469*	0.557*	−0.681**	−0.598**	0.005	−0.489*	0.697**	0.131	0.758**	0.672**	0.516*	0.306	0.582*
HREE	0.471*	0.221	0.511*	0.284	−0.623**	−0.730**	−0.357	−0.271	0.328	−0.003	0.510*	0.345	0.357	0.099	0.330

	Cu	Zn	Ga	Rb	Sr	Nb	Cs	Ba	Th	U	Zr	Hf	Yb	∑REE	LREE	HREE
Al_2O_3																
SiO_2																
TiO_2																
TFe_2O_3																
MnO																
CaO																
MgO																
Na_2O																
K_2O																
P_2O_5																
Sc																
V																
Cr																
Co																
Ni																
Cu	1															
Zn	0.333	1														
Ga	0.455	0.932**	1													
Rb	0.370	0.898**	0.977**	1												
Sr	−0.079	−0.125	0.131	0.212	1											
Nb	0.080	0.647**	0.511*	0.465	−0.325	1										
Cs	0.485*	0.748**	0.886**	0.927**	0.399	0.320	1									
Ba	0.235	−0.036	−0.053	−0.012	−0.080	0.109	0.071	1								
Th	0.122	0.845**	0.779**	0.811**	0.032	0.604**	0.742**	0.085	1							
U	0.087	0.631**	0.594**	0.616**	−0.039	0.181	0.532*	0.007	0.668**	1						
Zr	−0.139	−0.155	−0.373	−0.472*	−0.593**	0.299	−0.514*	0.219	−0.117	−0.256	1					
Hf	−0.097	−0.099	−0.318	−0.417	−0.578*	0.330	−0.449	0.233	−0.054	−0.234	0.995**	1				
Yb	0.235	0.759**	0.625**	0.594**	−0.356	0.868**	0.487*	0.205	0.820**	0.393	0.279	0.328	1			
∑REE	0.127	0.904**	0.799**	0.813**	−0.124	0.735**	0.692**	0.085	0.941**	0.701**	−0.095	−0.044	0.860**	1		
LREE	0.128	0.914**	0.816**	0.831**	−0.098	0.715**	0.710**	0.075	0.941**	0.714**	−0.124	−0.072	0.840**	0.999**	1	
HREE	0.096	0.687**	0.526*	0.529*	−0.369	0.840**	0.417	0.179	0.809**	0.477*	0.211	0.248	0.952**	0.880**	0.857**	1

Table 5 Ratios table of selected major and trace elements of the mudstones

Sample	ZP-01	ZP-02	ZP-03	ZP-04	ZP-05	ZP-06	ZP-07	ZP-08	ZP-09	ZP-10	ZP-11	ZP-12	ZP-13	ZP-14	ZP-15	ZP-16	ZP-17	ZP-18	Average	Max	Min
K_2O/Al_2O_3	0.20	0.23	0.21	0.20	0.19	0.17	0.16	0.18	0.13	0.16	0.19	0.21	0.22	0.20	0.19	0.25	0.17	0.21	0.19	0.25	0.13
SiO_2/Al_2O_3	2.82	2.73	2.98	2.70	3.99	5.22	6.77	3.69	8.53	5.24	2.80	2.82	3.09	2.66	3.21	2.91	6.71	5.37	4.12	8.53	2.66
K_2O/Na_2O	3.81	4.89	2.75	4.06	2.27	1.48	1.28	2.94	0.79	1.09	1.55	3.41	4.59	2.88	3.78	3.33	1.20	1.57	2.65	4.89	0.79
Al_2O_3/TiO_2	27.98	26.36	24.70	27.20	21.75	15.92	16.40	22.57	16.42	18.82	23.50	32.89	23.27	29.71	24.44	24.15	13.55	15.84	22.53	32.89	13.55
Sr/Ba	0.65	0.63	0.60	0.52	0.53	0.49	0.19	0.52	1.04	0.25	0.82	1.23	0.86	1.77	1.13	0.83	2.52	1.47	0.89	2.52	0.19
Sr/Cu	6.01	8.65	5.16	5.35	4.71	5.57	4.49	5.93	13.04	4.95	3.38	12.85	12.38	14.74	16.51	16.04	18.71	12.89	9.52	18.71	3.38
V/Cr	1.27	1.17	1.27	1.15	1.10	0.79	0.93	1.22	0.77	0.98	1.14	1.81	1.13	1.23	1.13	1.14	0.82	0.89	1.11	1.81	0.77
Ni/Co	6.02	4.74	3.61	4.74	3.55	4.27	3.16	3.67	4.20	3.16	4.03	3.81	5.36	4.62	4.41	3.51	4.27	4.58	4.20	6.02	3.16
Th/Sc	1.19	0.91	0.85	1.08	1.16	1.06	1.41	1.23	1.58	1.50	0.72	1.36	1.14	1.05	1.18	1.00	1.18	1.09	1.15	1.58	0.72
Zr/Sc	8.31	7.96	9.14	8.90	12.42	17.19	22.92	11.86	34.72	20.43	8.43	8.19	9.39	8.38	10.23	9.11	16.40	11.86	13.10	34.72	7.96
Co/Th	0.55	1.13	1.25	0.71	0.95	1.10	0.82	0.75	0.64	0.77	1.38	0.72	0.76	0.87	0.79	1.21	1.00	1.11	0.92	1.38	0.55
La/Sc	2.50	2.33	2.10	2.45	2.72	2.87	3.46	2.75	3.78	3.08	1.70	2.80	2.46	2.24	2.48	2.57	3.18	2.76	2.68	3.78	1.70
Ti/Zr	32.22	34.17	31.52	30.97	26.30	24.95	19.44	27.18	13.27	19.15	33.77	32.00	32.67	31.49	29.27	36.93	31.01	35.47	28.99	36.93	13.27

more than 1, except sample ZP17-01, which has an ICV value of 0.97 (Table 1). Based on these values, it can be inferred that the rocks have a minimal clay content and the sediment is compositionally immature.

The SiO_2/Al_2O_3 ratios depend on sediment recycling and weathering processes, indicating sediment maturity. The average ratio of SiO_2/Al_2O_3 greater than 5.0 indicates progressive maturity sediment (Potter, 1978; Roser et al., 1996; Madukwe et al., 2016; Shekhar et al., 2018). The SiO_2/Al_2O_3 ratios of our samples vary from 2.66 to 8.53 (Table 5), indicating an intermediate maturity level, which can be compared with the ICV values.

Alternatively, the Th/Sc and Zr/Sc ratios are further used to infer the degree of sedimentary recycling (McLennan et al., 1995; Bai et al., 2015; Qiu et al., 2015; Chen et al., 2020). As recycling progresses, there is a notable increase in Zr/Sc, while Th/Sc remains stable (McLennan et al., 1993; Li et al., 2022a). The Th/Sc ratios in our samples range from 0.72 to 1.58 while the Zr/Sc ratios range from 7.96 to 34.72 (Table 5). As shown in the Zr/Sc-Th/Sc diagram (Fig. 4), the data spots corresponding to all mudstones are relatively concentrated and exhibit a weak sedimentary recycling trend, which suggests insignificant recycling with an initial depositional environment.

The chemical index of alteration (CIA) has been commonly used to estimate the intensity of chemical weathering in the source region (Nesbitt and Young, 1982). The formula can be shown as CIA = $[Al_2O_3 / [Al_2O_3 + CaO^* + Na_2O + K_2O] \times 100$, with all the elements expressed in molecular percentages. Here, CaO* represents the amount incorporated in the silicate fraction of the rock, defined as $CaO^* = CaO - 10/3 \times P_2O_5$ (McLennan et al., 1993). The CIA values between 50 and 60 represent a low degree of chemical weathering in cold, dry climates. A range of 60−80 indicates moderate weathering, which is typical of warm, humid conditions. Finally, values ranging from 80 to 100 represent intense

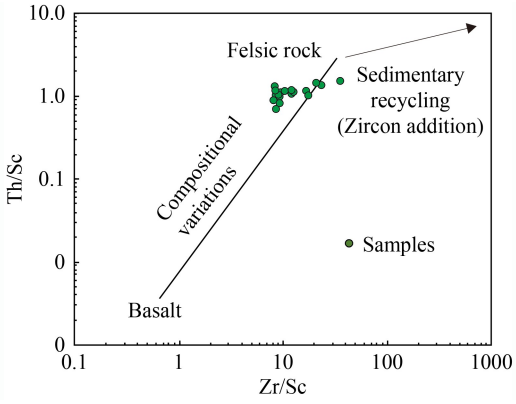

Fig. 4 Diagram of Zr/Sc versus Th/Sc for the mudstone samples.

weathering observed in hot, humid tropical-subtropical climates, indicating that the parent rock has undergone substantial weathering (Nesbitt and Young, 1982; Fedo et al., 1995; Bock et al., 1998; Xu and Shao, 2018). The CIA values of the mudstone samples are given in Table 1. They range between 59.79 and 72.90 with an average of 66.70, indicating that the Niubao Formation mudstones suffered from low to moderate weathering. As depicted on the A-CN-K (Al_2O_3-CaO + Na_2O-K_2O) ternary diagram, the mudstone samples show an evolution trend from the upper crust to kaolinite along the A-CN axis (Fig. 5). Even though the samples also deviate from the ideal weathering trend (IWT) and are inclined toward illite, which could be attributed to K-metasomatism during diagenesis (Fedo et al., 1995; Michalopoulos and Aller, 1995), the subtle divergence of samples implies a weak diagenetic impact (Ma et al., 2015).

5.2 Paleoenvironmental conditions

5.2.1 Paleosalinity and paleoclimate

The Sr/Ba ratios are a diagnostic indicator for

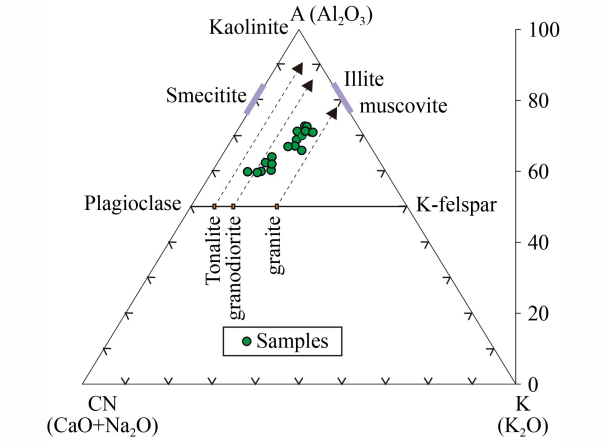

Fig. 5 A-CN-K ternary plot and associated chemical index of alteration (CIA) variation. Dashed lines represent the ideal weathering trends of tonalite, granodiorite, and granite, respectively (Fedo et al., 1995).

determining paleosalinity and paleoclimate variations. High Sr/Ba ratios, typically above 1.0, signify water columns with high salinity prevalent in arid climatic settings, whereas values less than 0.5 represent water columns with low salinity associated with humid climatic conditions (Meng et al., 2012; Fu et al., 2016; Wang et al., 2017a). Among the analyzed samples, six samples had values more than 1, while two samples had values less than 0.5 (Table 5; Fig. 2), potentially highlighting variation in paleosalinity over time and the transient dry and humid climate change of the sedimentary environment. In addition, Sr/Cu ratios less than 5.0 are indicative of humid climate conditions, whereas those exceeding 5.0 are characteristic of arid climate conditions (Lerman, 1989; Meng et al., 2012; Jia et al., 2013; Liang et al., 2014; Cao et al., 2015; Fu et al., 2016, 2018). The Sr/Cu ratio was close to 5.0 for four samples, over 5 for all other samples, and greater than 12 for most of the samples, indicating relatively dry climate conditions (Table 5).

Certain elements, such as V, Co, and Cu, are recognized as redox-sensitive and commonly accumulate in anoxic sediments (Algeo and Maynard, 2004; Tribovillard et al., 2006; Lézin et al., 2013; Ayinla et al., 2017). Key trace element ratios, such as V/Cr and Ni/Co ratios, are reliable indicators of redox conditions. The V/Cr ratios, which typically increase with decreasing oxygen content in a water column, can be used to classify environments: ratios less than 2.0 suggest oxic conditions, those between 2.0 and 4.25 indicate dysoxic conditions, and values above 4.25 signify anoxic conditions (Jones and Manning, 1994). The V/Cr ratios of the mudstones fluctuate from 0.77 to 1.81 (Table 5; Fig. 2), indicating oxic conditions. Similarly, Ni/Co ratio values less than 5.0 indicate an oxidizing environment, values between 5.0 and 7.0 suggest suboxic to dysoxic conditions, and values over 7.0 indicate reducing conditions (Jones and Manning, 1994). Our mudstone samples have Ni/Co ratios between 3.16 and 6.02 (Table 5; Fig. 2), further supporting oxic conditions during deposition.

5.2.2 Mean average temperature (MAT) calculation

Chemical weathering processes are significantly influenced by climatic factors (Nesbitt and Young, 1982). In the weathering of granitic bedrock soils, the sodium depletion fraction index (τNa) effectively indicates terrestrial chemical weathering intensity (Gaillardet et al., 1999; Anderson et al., 2002; Rasmussen et al., 2011; West, 2012; Garzanti et al., 2013). The intensity of chemical weathering in the topsoil of weathered granite bedrock shows a positive correlation with the mean annual surface temperature (MAT) in modern non-glacial areas (Yang et al., 2016). The empirical equation can express this relationship: MAT = −24.2τNa−0.9 (r^2 = 0.84, P < 0.0001). Four specific criteria must be considered before employing this equation. First, annual precipitation should range between 400 mm and 4000 mm, avoiding extreme aridity or excessive humidity conditions. Secondly, the source rock should be felsic igneous rocks. Thirdly, the physical erosion rate should be 2−100 m/m.y. Fourthly, sorting and sedimentary recycling processes during transport need to be comparatively weak, and finally, diagenetic processes should be minimal.

Evidence from late Eocene fossils suggests the presence of tropical to subtropical climates (Fang et al., 2020). The diagram of Zr vs TiO_2 for the samples points out that the mudstones predominantly originate from the felsic igneous rocks source area (Fig. 6(b)). Furthermore, the erosion rate in the central regions of the plateau during the Eocene (~45 Ma) was below 50 m/m.y (Rohrmann et al., 2012). It is coupled with weak recycling effects (Fig. 4) and the absence of diagenetic

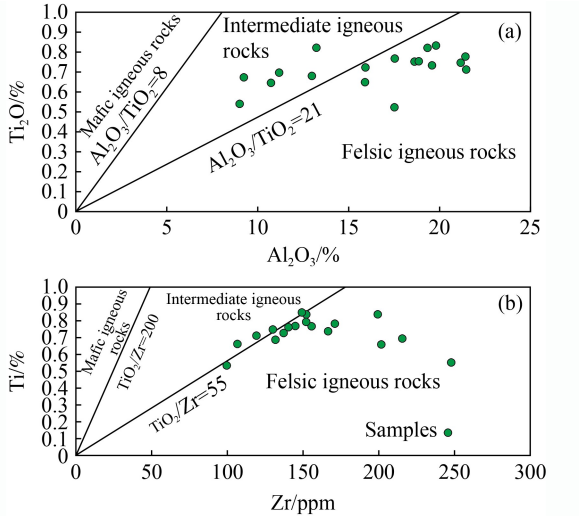

Fig. 6 (a) Diagram of Al_2O_3 versus TiO_2 for the mudstone samples. (b) Diagram of Zr versus TiO_2 for the mudstone samples.

alteration minerals, which conform to the application conditions of the empirical formula. Using granite and granodiorite as the original rock (Chi, 2007), the τNa of 18 mudstone samples spans from 0.93 to 2.42 with an average of 1.34. These results suggest that the average land surface temperature during the late Eocene is estimated to be 11.64°C ± 4.19°C (Table 1; Fig. 2).

The carbonate formation temperature of paleosol carbonates derived from clumped isotope analysis can represent the surface temperature during formation (Ghosh et al., 2006). The carbonate formation temperatures in the upper member of the Niubao Formation range between 10.1°C and 12.9°C, with an average of 11.9°C and a standard deviation of 2.8°C (Xiong et al., 2022). Ingalls et al. (2020) interpreted the $T(\Delta 47)$ values of ~30°C to 36°C in soil carbonate in the late Eocene to Oligocene upper Niubao Formation in the Lunpola Basin as the maximum possible surface temperature during summer. It has been shown that terrestrial soil carbonates recorded $T(\Delta 47)$ values approximately 18°C warmer than MAT at midlatitudes during the Paleocene-Eocene (Snell et al., 2013). Thus, the findings suggest an annual average temperature of 12°C to 18°C during the late Eocene to Oligocene.

The numerical climate modeling and proxy thermal regimes yield consistent results, indicating a shift toward a drier and cooler climate in central Xizang during the mid-late Eocene (Su et al., 2019; Chen et al., 2021; Zhang et al., 2022). The presence of multiple animal fossils alongside a diverse grass community, palms, and a variety of other woody species suggests the existence of a subtropical open woodland ecosystem, with an estimated dry bulb mean annual temperature of ~15.6°C (Deng et al., 2012; Wu et al., 2017; Wang et al., 2018b; Mao et al., 2019; Del Rio et al., 2020; Xu et al., 2022; Zhang et al., 2022).

In summary, the paleotemperature inferred from the geochemical proxies in mudstones in the Nima Basin is in concordance with the results obtained from paleontological and isotopic investigations, providing support for the hypothesis that the central plateau exhibited a cooler climatic regime during the late Eocene.

5.3 Source lithotypes and tectonic setting

5.3.1 Source lithotypes

The REE parameters are relative to the sources of sedimentary rocks due to their high stability during weathering, erosion, and early diagenesis (McLennan et al., 1995; Bock et al., 1998; Asiedu et al., 2000; Cullers and Podkovyrov, 2000; Kasanzu et al., 2008; Armstrong-Altrin et al., 2009). Generally, negative Eu anomalies reflect felsic rocks, whereas minimal or no Eu anomalies mainly indicate mafic rocks (Roddaz et al., 2006; Kasanzu et al., 2008; Armstrong-Altrin et al., 2017). The distribution patterns of mudstone samples chondrite-normalized REEs are relatively consistent, indicating that the mudstones originated from the same source. The REE profiles of the mudstones also exhibit significant negative Eu anomalies (Fig. 3(c)), strongly indicating that the mudstones were derived from felsic rocks. Additionally, the REE exhibit a negative correlation with CaO (R^2 = 0.617; Table 3), indicating that the REE concentrations in the mudstone samples are predominantly controlled by terrigenous material (Zeng et al., 2020).

The geochemical compositions of detrital deposits provide vital insights into their provenance (Wesolowski, 1992; Ayers and Watson, 1993; Cullers and Podkovyrov, 2000; Verma and Armstrong-Altrin, 2013, 2016; Armstrong-Altrin et al., 2013, 2015a, 2015b, 2017; Madhavaraju, 2015). The Al_2O_3/TiO_2 ratio in clastic sediments is widely considered an effective indicator of the lithology of sedimentary source rocks. Mafic rocks have Al_2O_3/TiO_2 ratios ranging from 3 to 8, intermediate rocks have ratios ranging from 8 to 21, and felsic rocks have ratios ranging from 21 to 70 (Hayashi et al., 1997; Armstrong-Altrin et al., 2015a, 2017; Zhou et al., 2015; Moradi et al., 2016; Verma and Armstrong-Altrin, 2016; Wang et al., 2017b). The ratios of our samples range from 13.55 to 32.89, averaging 22.53 (Table 5; Fig. 6(a)). Most samples exhibit values characteristic of felsic rocks, while only six samples display values associated with intermediate rocks. Similarly, the TiO_2/Zr ratio can be used to investigate the origin of sediments. A TiO_2/Zr ratio up to 200 suggests that the sediments originated from the erosion of mafic rocks. Alternatively, ratios between 55 and 200 are indicative of intermediate igneous rock sources, and ratios less than 55 are indicative of felsic igneous rock sources (Hayashi et al., 1997; Zeng et al., 2020; Kirubakaran et al., 2023). The Zr-TiO_2 graph (Fig. 6(b)) and the Al_2O_3 vs TiO_2 (Fig. 6(a)) diagram for the mudstone samples indicate a predominance of felsic igneous source rocks and subordinate intermediate igneous source rocks.

The Co/Th ratio is a distinctive indicator of felsic versus mafic sources, as felsic rocks typically exhibit lower Co/Th values than mafic rocks (Amorosi et al., 2002; Cullers, 2002). Our collected samples feature Co/Th values between 0.55 and 1.37, which are notably lower than the benchmarks of the UCC (1.65) and PAAS (1.37), suggesting a predominantly felsic source (Table 5; Ma et al., 2015). Similarly, the La/Sc ratio has been recognized as a reliable source composition indicator (Floyd and Leveridge, 1987; Condie, 1993; McLennan et al., 1995; Gu et al., 2002; Ma et al., 2015). T he La/Sc-Co/Th plot (Fig. 7(a)) reveals that the samples are predominantly concentrated between granodiorite and adamellite. Additionally, on the Zr/Sc-Th/Sc plot (Fig. 7(b)), the majority of the data plot in the felsic source area.

In conclusion, geochemical results suggest that the mudstones of the Niubao Formation predominantly

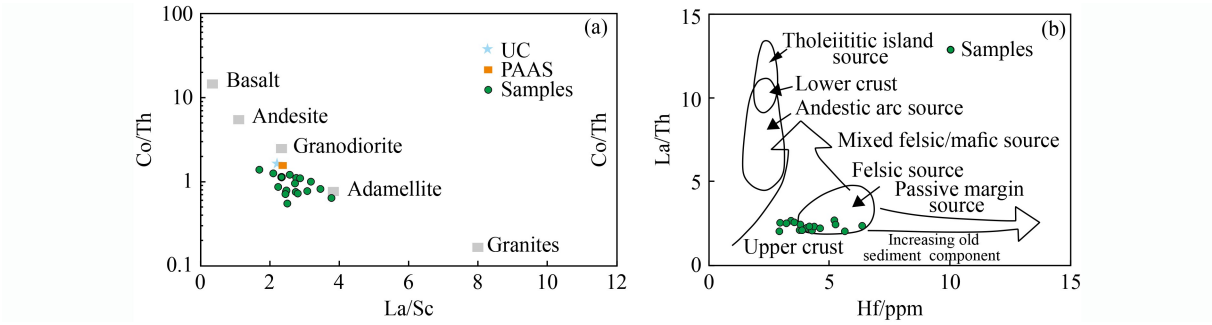

Fig. 7 (a) Diagram of La/Sc versus Co/Th for the mudstone samples. The various igneous rock data were extracted from Condie (1993). (b) Diagram of Hf - versus - La/Th for the mudstones.

originated from the source area of felsic rocks with abundant felsic igneous rocks and minor intermediate igneous rocks.

5.3.2 Tectonic setting

The geochemical characteristics of sedimentary rocks could reveal the composition and tectonic setting of source rocks (Bhatia and Crook, 1986; Roser and Korsch, 1988). Clastic sediments from various tectonic environments can exhibit unique terrane-specific imprints, leading to diverse geochemical compositions (Roser et al., 1996; Bai et al., 2015).

The discriminant function diagram illustrates the mudstones plotted in the collision area (Fig. 8; Verma and Armstrong-Altrin, 2013). The La-Th-Sc plot (Fig. 9(a)) shows that most of mudstone samples cluster within and near the edges of the continental island arc field. In the Th-Sc-Zr/10 plot (Fig. 9(b)), there is an observable spread of sample points, with most of them positioned in the continental island arc and a few scattered within the passive margin. The Th-Co-Zr/10 diagram (Fig. 9(c)) displays some mudstone samples within the continental island arc field, while others gravitate toward the boundaries of the active continental margin. In addition, the mudstones have high ΣREE values (124.81−204.83 ppm), $(La/Yb)_N$ ratios (8.47−10.99), and negative Eu anomalies (Eu/Eu* values ranging from 0.59 to 0.70) reinforce the conclusion of the continental island arc (Bhatia and Crook, 1986; Table 4).

5.4 Provenance interpretation

As an intermontane basin proposed by previous work, it

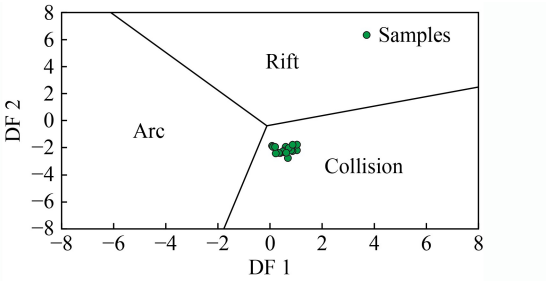

Fig. 8 Discriminant function diagram illustrating the tectonic setting of the Niubao Formation (Verma and Armstrong-Altrin, 2013). DF1 = (0.608 × ln(TiO_2/SiO_2)) + (− 1.854 × ln(Al_2O_3/SiO_2)) + (0.299 × ln(Fe_2O_3/SiO_2)) + (− 0.550 × ln(MnO/SiO_2)) + (0.120 × ln(MgO/SiO_2)) + (0.194 × ln(CaO/SiO_2)) + (− 1.510 × ln(Na_2O/SiO_2) + (1.941 × ln(K_2O/SiO_2)) + (0.003 × ln(P_2O_5/SiO_2))−0.294; and DF2 = (− 0.554 × ln(TiO_2/SiO_2)) + (− 0.995 × ln(Al_2O_3/SiO_2)) + (1.765 × ln(Fe_2O_3/SiO_2)) + (− 1.391 × ln(MnO/SiO_2)) + (− 1.034 × ln(MgO/SiO_2)) + (0.225 × ln(CaO/SiO_2) + (0.713 × ln(Na_2O/SiO_2) + (0.330 × ln(K_2O /SiO_2)) + (0.637 × ln(P_2O_5/SiO_2)) − 3.631.

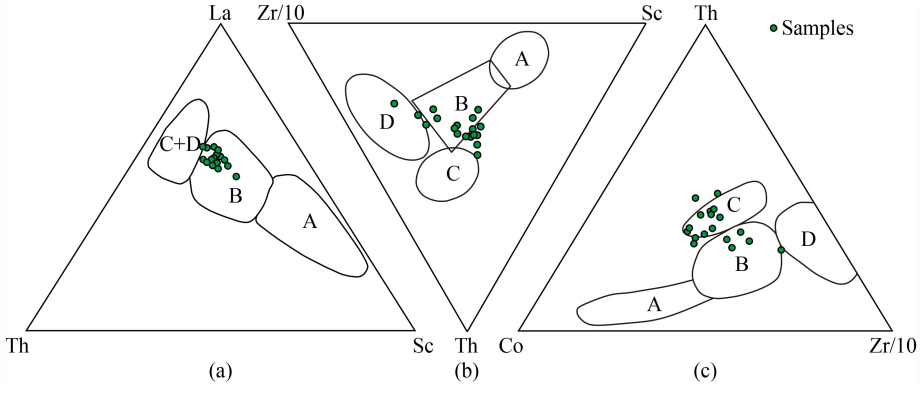

Fig. 9 (a) La-Th-Sc plot for mudstone samples. (b) Th-Sc-Zr/10 plot of mudstone samples. (c) Th-Co-Zr/10 plot for the mudstone samples. (A: Oceanic island arc; B: Continental island arc; C: Active continental margin; D: Passive margin. Bhatia and Crook, 1986; Basu et al., 2016).

is reasonable to speculate that the neighboring geological units fed the Niubao Formation in the Nima Basin, namely the southern Qiangtang, the northern Lhasa, and the BNSZ (Rowley et al., 2015; Mi et al., 2018; Han et al., 2022), which are characterized by widely distributed pre-Cenozoic felsic and intermediate igneous rocks, particularly Cretaceous and Jurassic in age (Chapman and Kapp, 2017). According to the detrital zircon U-Pb age distributions of the Niubao Formation, zircons originating from these igneous rocks are the predominant components of the distinct peaks (Kapp et al., 2007; Donaldson et al., 2013; Zhu et al., 2017; Li et al., 2022b; Liu et al., 2023). Several representative intrusive and volcanic rocks are compared to the trace elements and REE of the mudstone samples (Lee et al., 2012; Li et al., 2013; Wang et al., 2014b; Li et al., 2016; Yan et al., 2016; Chen et al., 2017; Hu et al., 2017; Liu et al., 2017). Figure 10(a) displays that the Cretaceous and Jurassic granodiorites from Amdo and the southern Qiangtang, along with the mudstone samples, show

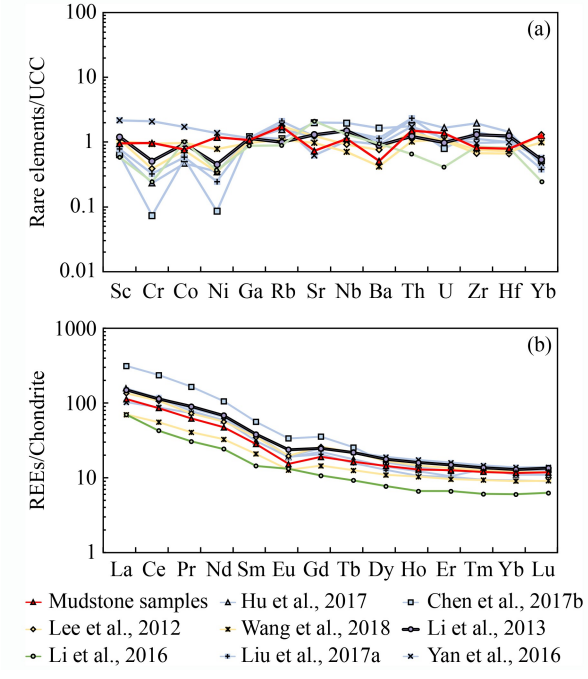

Fig. 10 (a) Diagram comparing the upper continental crust-normalized rare elements (REEs) of mudstones from the Nima Basin with those of their source igneous rock. (b) Diagram comparing the chondrite-normalized rare earth element of mudstones from the Nima Basin with those of their source igneous rock (data from Lee et al. (2012): the Cretaceous volcanic rocks in the northern Lhasa. Li et al. (2013): the Cretaceous Abushan volcanic rocks in the southern Qiangtang. Wang et al. (2014b): the Cretaceous andesites and dacites in the northern Lhasa. Li et al. (2016): the Late Jurassic granodiorites in Kangqiong. Yan et al. (2016): the Early-Middle Jurassic Calc-alkaline granodiorite in Amdo. Chen et al. (2017): the Late Cretaceous alkaline andesites in Amdo. Hu et al. (2017): the Early Cretaceous granodiorites in Zigetang Co. Liu et al. (2017): the Early Cretaceous mica granites in Amdo).

enrichment in Th and U elements relative to the upper crust. In contrast, the volcanic rocks on the west side of the Nima Basin do not show similar enrichment. In addition, the REE concentrations in the volcanic rocks from the west of the Nima Basin are lower than in the mudstone samples (Fig. 10(b)), suggesting that the volcanic rocks on the west side of the Nima Basin are unlikely geochemically related to the mudstones. Beyond that, the abundance of limestone clasts in the conglomerates of the Niubao Formation is indicative that the extensively distributed Mesozoic marine strata of the southern Qiangtang and northern Lhasa terranes also contributed an enormous amount of debris to the Niubao Formation (Han et al., 2019; Kong et al., 2019; Liu et al., 2023).

5.5 Palaeogeography of the drainage basin and implications for the landscape evolution

The increasing amount of quantitative paleoaltitude data sets based on various methods suggests a lowland valley with an elevation of 2−3 km during the Eocene, which ran between the highlands of the Gangdese arc (Currie et al., 2005; Ding et al., 2014; Currie et al., 2016) to the south and the central Qiangtang terrane to the north (Zhu et al., 2013, 2015; Wu et al., 2017; Su et al., 2019; Fang et al., 2020; Ding et al., 2022; Li et al., 2022c; Xiong et al., 2022; Bi et al., 2023). However, the west of central Xizang was near sea level during the late Eocene (Wei et al., 2016). Apatite fission track studies suggest that the Amdo area, a few hundred kilometres east of the Nima Basin, underwent rapid cooling in the early Cretaceous times (ca. 110 Ma; Bi et al., 2023; Lu et al., 2024). Low temperature thermochronological data demonstrated that the west of the Nima Basin did not experience rapid cooling until the late Cretaceous (ca. 70 Ma; Xue et al., 2022). On the basis of the differential cooling history, it is possible that the land surface uplift in the eastern portion of central Xizang commenced prior to that in the western portion, thereby establishing an elevation gradient from eastern highlands to western lowlands. The early Cenozoic sedimentary basins along the BNSZ accumulate several kilometres thick of fluvial-lacustrine sediments and show great similarities in sedimentary structural characteristics and sedimentary facies. It could be inferred that these basins may have been interconnected (e.g., Ma et al., 2015; Han et al., 2019). Furthermore, the westward direction of paleocurrents in the Lunpola and Bangoin basins suggests the possibility of a drainage system extending from east to west across the central part of the Xizang Plateau (He et al., 2012; Ma et al., 2015; Han et al., 2019). Hence, a westward drained source-to-sink system likely developed since the Cenozoic. In this geomorphologic pattern, it makes more sense that the mudstones of the Nima Basin have a stronger affinity for

the igneous rocks to their east.

6 Conclusions

The geochemical analysis of the late Eocene of the Niubao Formation was undertaken to study the paleoclimate conditions, provenance, and tectonic settings. The main conclusions are summarized as follow.

1) The Niubao Formation mudstones are characterized by high contents of SiO_2, Al_2O_3, and CaO and are primarily composed of clay minerals.

2) The mudstone samples have a total rare earth element (ΣREE) content of 124.81−204.83 ppm. They exhibit a higher proportion of light rare earth elements (LREEs) compared to heavy rare earth elements (HREEs) and display notable negative Eu anomalies.

3) The sediment is first recycled and compositionally immature. The CIA values (59.8−72.9) indicate that the source area of the Niubao Formation experienced moderate chemical weathering.

4) The mudstones were deposited in an oxidizing and arid depositional environment with a mean annual temperature (MAT) of 11.64°C ± 4.19°C, reflecting a cool environmental conditions in central Xizang during the late Eocene.

5) The mudstones were predominantly derived from felsic and intermediate igneous rocks that originated in a continental island arc setting. Igneous rocks from the north, south, and east of the Nima Basin contributed significantly to the composition of these mudstones.

6) Combining data of paleoaltimetry and low temperature thermochronology, the geochemical characteristics of the Niubao Formation suggest the possible development of a westward-draining source-to-sink system since the Cenozoic.

Acknowledgments This work was supported by the Second Xizang Plateau Scientific Expedition Program (No. 2019QZKK0803), National Natural Science Foundation of China (Grant Nos. 42172113 and 41802124), Fundamental Research Funds for the Central Universities (No. 265202138), "Deep-time Digital Earth" Science and Technology Leading Talents Team Funds for the Central Universities for the Frontiers Science Center for Deep-time Digital Earth, China University of Geosciences (Beijing) (No. 2652023001), and Key Laboratory of Sedimentary Basin and Oil and Gas Resources, Ministry of Natural Resources of the PRC (No. cdcgs2018006).

Competing interests The authors declare that they have no competing interests.

References

Algeo T J, Maynard J B (2004). Trace-element behavior and redox facies in core shales of Upper Pennsylvanian Kansas-type cyclothems. Chem Geol, 206(3−4): 289–318

Amorosi A, Centineo M C, Dinelli E, Lucchini F, Tateo F (2002). Geochemical and mineralogical variations as indicators of provenance changes in Late Quaternary deposits of SE Po Plain. Sediment Geol, 151(3−4): 273–292

Amorosi A, Sammartino I, Dinelli E, Campo B, Guercia T, Trincardi F, Pellegrini C (2022). Provenance and sediment dispersal in the Po-Adriatic source-to-sink system unraveled by bulk-sediment geochemistry and its linkage to catchment geology. Earth Sci Rev, 234: 104202

Anderson S P, Dietrich W E, Brimhall G H Jr (2002). Weathering profiles, mass-balance analysis, and rates of solute loss: linkages between weathering and erosion in a small, steep catchment. Geol Soc Am Bull, 114(9): 1143–1158

Armitage J J, Duller R A, Whittaker A C, Allen P A (2011). Transformation of tectonic and climatic signals from source to sedimentary archive. Nat Geosci, 4(4): 231–235

Armstrong-Altrin J S, Lee Y I, Kasper-Zubillaga J J, Trejo-Ramírez E (2017). Mineralogy and geochemistry of sands along the Manzanillo and El Carrizal beach areas, southern Mexico: implications for palaeoweathering, provenance and tectonic setting. Geol J, 52(4): 559–582

Armstrong-Altrin J S, Lee Y I, Verma S P, Worden R H (2009). Carbon, oxygen, and strontium isotope geochemistry of carbonate rocks of the upper Miocene Kudankulam Formation, southern India: implications for paleoenvironment and diagenesis. Chem Erde, 69(1): 45–60

Armstrong-Altrin J S, Machain-Castillo M L, Rosales-Hoz L, Carranza-Edwards A, Sanchez-Cabeza J A, Ruíz-Fernández A C (2015a). Provenance and depositional history of continental slope sediments in the Southwestern Gulf of Mexico unraveled by geochemical analysis. Cont Shelf Res, 95: 15–26

Armstrong-Altrin J S, Nagarajan R, Balaram V, Natalhy-Pineda O (2015b). Petrography and geochemistry of sands from the Chachalacas and Veracruz beach areas, western Gulf of Mexico, Mexico: constraints on provenance and tectonic setting. J S Am Earth Sci, 64: 199–216

Armstrong-Altrin J S, Nagarajan R, Madhavaraju J, Rosalez-Hoz L, Lee Y I, Balaram V, Cruz-Martínez A, Avila-Ramírez G (2013). Geochemistry of the Jurassic and Upper Cretaceous shales from the Molango Region, Hidalgo, eastern Mexico: implications for source-area weathering, provenance, and tectonic setting. C R Geosci, 345(4): 185–202

Asiedu D K, Suzuki S, Nogami K, Shibata T (2000). Geochemistry of Lower Cretaceous sediments, inner zone of Southwest Japan: constraints on provenance and tectonic environment. Geochem J, 34(2): 155–173

Ayers J C, Watson E B (1993). Rutile solubility and mobility in supercritical aqueous fluids. Contrib Mineral Petrol, 114(3): 321–330

Ayinla H A, Abdullah W H, Makeen Y M, Abubakar M B, Jauro A, Sarki Yandoka B M, Zainal Abidin N S (2017). Petrographic and geochemical characterization of the Upper Cretaceous coal and mudstones of Gombe Formation, Gongola sub-basin, northern Benue trough Nigeria: implication for organic matter preservation, paleodepositional environment and tectonic settings. Int J Coal Geol, 180: 67–82

Bai Y Y, Liu Z J, Sun P C, Liu R, Hu X F, Zhao H Q, Xu Y B (2015). Rare earth and major element geochemistry of Eocene fine-grained sediments in oil shale-and coal-bearing layers of the Meihe Basin, Northeast China. J Asian Earth Sci, 97: 89–101

Banerji U S, Dubey C P, Goswami V, Joshi K B (2022). Geochemical indicators in provenance estimation. In: Geochemical Treasures and Petrogenetic Processes. Singapore: Springer Nature Singapore, 95–121

Barshad I (1966). Factors affecting the frequency distribution of clay minerals in soils. Clays and Clay Minerals, 1966: 207

Basu A, Bickford M E, Deasy R (2016). Inferring tectonic provenance of siliciclastic rocks from their chemical compositions: a dissent. Sediment Geol, 336: 26–35

Bhatia M R (1983). Plate tectonics and geochemical composition of sandstones. J Geol, 91(6): 611–627

Bhatia M R, Crook K A (1986). Trace element characteristics of graywackes and tectonic setting discrimination of sedimentary basins. Contrib Mineral Petrol, 92(2): 181–193

Bi W J, Li Y L, Kamp P J J, Xu G Q, Zhang J W, Han Z P, Du L T, Wang C S, He H Y, Xu T K, Ma Z N (2023). Cretaceous–Cenozoic cooling history of the Qiangtang terrane and implications for Central Xizang formation. Geol Soc Am Bull, 135(5−6): 1587–1601

Bock B, McLennan S M, Hanson G N (1998). Geochemistry and provenance of the middle Ordovician Austin Glen member (Normanskill formation) and the Taconian orogeny in New England. Sedimentology, 45(4): 635–655

Botsyun S, Sepulchre P, Donnadieu Y, Risi C, Licht A, Caves Rugenstein J K (2019). Revised paleoaltimetry data show low Xizang Plateau elevation during the Eocene. Science, 363(6430): eaaq1436

Cao H S, Guo W, Shan X L, Ma L, Sun P C (2015). Paleolimnological environments and organic accumulation of the Nenjiang Formation in the Southeastern Songliao Basin, China. Oil Shale, 32(1): 5–24

Caracciolo L (2020). Sediment generation and sediment routing systems from a quantitative provenance analysis perspective: review, application and future development. Earth Sci Rev, 209: 103226

Cerling T E, Harris J M, MacFadden B J, Leakey M G, Quade J, Eisenmann V, Ehleringer J R (1997). Global vegetation change through the Miocene/Pliocene boundary. Nature, 389(6647): 153–158

Chapman J B, Kapp P (2017). Xizang magmatism database. Geochem Geophys Geosyst, 18(11): 4229–4234

Chen L, Chen X H, Zhang B M, Zhang G T, Li H, Lin W B, Chen P, Hu H Y, Tian W (2020). Provenance and palaeoenvironment of Upper Devonian Shetianqiao Formation mudstones in Shaoyang Sag, Xiangzhong Depression, Central China. Geol J, 55(1): 934–948

Chen S S, Fan W M, Shi R D, Gong X H, Wu K (2017). Removal of deep lithosphere in ancient continental collisional orogens: a case study from central Xizang, China. Geochem Geophys Geosyst, 18(3): 1225–1243

Chen X Q, Xing F C, Jiang S, Lu Y C, Liu Z R, Pan L, Hu H R (2021). Origin and formation model of Eocene dolomite in the upper Niubao Formation of the Lunpola Basin, Xizang Plateau. Interpretation (Tulsa), 9(3): SF11–SF22

Chen Y, Yi H S, Xia G Q, Yi F, Tang W Q, Li G J, Wu X H, Shi Y X (2022). The organic geochemical characteristics from the Palaeogene lacustrine source rock in the Nyima Basin, Central Xizang, and their geological significance. Geol J, 57(3): 1186–1207

Chi Q H (2007). Handbook of Applied Geochemical Element Abundance Data. Beijing: Geological Press

Condie K C (1993). Chemical composition and evolution of the upper continental crust: contrasting results from surface samples and shales. Chem Geol, 104(1−4): 1–37

Cox R, Lowe D R, Cullers R L (1995). The influence of sediment recycling and basement composition on evolution of mudrock chemistry in the southwestern United States. Geochim Cosmochim Acta, 59(14): 2919–2940

Crichton J G, Condie K C (1993). Trace elements as source indicators in cratonic sediments: a case study from the Early Proterozoic Libby Creek Group, southeastern Wyoming. J Geol, 101(3): 319–332

Cullers R L (2002). Implications of elemental concentrations for provenance, redox conditions, and metamorphic studies of shales and limestones near Pueblo, CO, USA. Chem Geol, 191(4): 305–327

Cullers R L, Podkovyrov V N (2000). Geochemistry of the Mesoproterozoic Lakhanda shales in southeastern Yakutia, Russia: implications for mineralogical and provenance control, and recycling. Precambrian Res, 104(1−2): 77–93

Currie B S, Polissar P J, Rowley D B, Ingalls M, Li S, Olack G, Freeman K H (2016). Multiproxy paleoaltimetry of the late Oligocene-Pliocene Oiyug basin, southern Xizang. Am J Sci, 316(5): 401–436

Currie B S, Rowley D B, Tabor N J (2005). Middle Miocene paleoaltimetry of southern Xizang: implications for the role of mantle thickening and delamination in the Himalayan orogen. Geology, 33(3): 181–184

DeCelles P G, Kapp P, Ding L, Gehrels G E (2007a). Late Cretaceous to middle Tertiary basin evolution in the central Xizang Plateau: changing environments in response to tectonic partitioning, aridification, and regional elevation gain. Geol Soc Am Bull, 119(5−6): 654–680

DeCelles P G, Quade J, Kapp P, Fan M, Dettman D L, Ding L (2007b). High and dry in central Xizang during the Late Oligocene. Earth Planet Sci Lett, 253(3−4): 389–401

Del Rio C, Wang T X, Wu F X, Liang X Q, Spicer T E, Zhou Z K, Su T (2020). Fossil record of *Ceratophyllum* aff. *muricatum Cham*. (Ceratophyllaceae) from the middle Eocene of central Xizang Plateau, China. Rev Palaeobot Palynol, 281: 104284

Deng T, Ding L (2015). Paleoaltimetry reconstructions of the Xizang Plateau: progress and contradictions. Natl Sci Rev, 2(4): 417–437

Deng T, Wang S Q, Xie G P, Li Q, Hou S K, Sun B Y (2012). A mammalian fossil from the Dingqing Formation in the Lunpola Basin, northern Xizang, and its relevance to age and paleo-altimetry. Chin Sci Bull, 57(2−3): 261–269

Ding L, Kapp P, Cai F L, Garzione C N, Xiong Z Y, Wang H Q, Wang C (2022). Timing and mechanisms of Xizang Plateau uplift. Nat

Rev Earth Environ, 3(10): 652–667

Ding L, Xu Q, Yue Y H, Wang H Q, Cai F L, Li S (2014). The andean-type gangdese mountains: paleoelevation record from the paleocene-eocene Linzhou Basin. Earth Planet Sci Lett, 392: 250–264

Donaldson D G, Webb A A, Menold C A, Kylander-Clark A R, Hacker B R (2013). Petrochronology of Himalayan ultrahigh-pressure eclogite. Geology, 41(8): 835–838

Duddy L R (1980). Redistribution and fractionation of rare-earth and other elements in a weathering profile. Chem Geol, 30(4): 363–381

Dupont-Nivet G, Krijgsman W, Langereis C G, Abels H A, Dai S, Fang X (2007). Xizang plateau aridification linked to global cooling at the Eocene–Oligocene transition. Nature, 445(7128): 635–638

Fang X M, Dupont-Nivet G, Wang C S, Song C H, Meng Q Q, Zhang W L, Nie J S, Zhang T, Mao Z Q, Chen Y (2020). Revised chronology of central Xizang uplift (Lunpola Basin). Sci Adv, 6(50): eaba7298

Fedo C M, Wayne Nesbitt H, Young G M (1995). Unraveling the effects of potassium metasomatism in sedimentary rocks and paleosols, with implications for paleoweathering conditions and provenance. Geology, 23(10): 921–924

Feng W, Meng Q, Song C, Fang X, Zhuang G, He P, Yang S, Zhang J, Chen Y, Zhang Y (2023). Constraints on the timing of the India‐Asia collision and unroofing history of the Himalayan orogen using detrital zircon U‐Pb‐Hf and whole‐rock Sr‐Nd isotopes in Cretaceous‐Miocene Lesser Himalayan sedimentary rocks. Basin Res, 35(3): 949–977

Floyd P A, Leveridge B E (1987). Tectonic environment of the Devonian Gramscatho basin, south Cornwall: framework mode and geochemical evidence from turbiditic sandstones. J Geol Soc London, 144(4): 531–542

Fu X G, Wang J, Chen W B, Feng X L, Wang D, Song C Y, Zeng S Q (2016). Elemental geochemistry of the early Jurassic black shales in the Qiangtang Basin, eastern Tethys: constraints for palaeoenvironment conditions. Geol J, 51(3): 443–454

Fu X G, Wang J, Feng X L, Chen W B, Wang D, Song C, Zeng S Q (2018). Mineralogical compositions and elemental enrichment of shales in lacustrine rift basin: a case study in the Cenozoic Lunpola Basin, central Xizang. Geol J, 53(2): 439–457

Gaillardet J, Dupré B, Allègre C J (1999). Geochemistry of large river suspended sediments: silicate weathering or recycling tracer. Geochim Cosmochim Acta, 63(23−24): 4037–4051

Gallala W, Gaied M E, Montacer M (2009). Detrital mode, mineralogy and geochemistry of the Sidi Aïch Formation (Early Cretaceous) in central and southwestern Tunisia: implications for provenance, tectonic setting and paleoenvironment. J Afr Earth Sci, 53(4−5): 159–170

Garzanti E, Padoan M, Setti M, Najman Y, Peruta L, Villa I M (2013). Weathering geochemistry and Sr‐Nd fingerprints of equatorial upper Nile and Congo muds. Geochem Geophys Geosyst, 14(2): 292–316

Ghosh P, Adkins J, Affek H, Balta B, Guo W, Schauble E A, Schrag D, Eiler J M (2006). ^{13}C–^{18}O bonds in carbonate minerals: a new kind of paleothermometer. Geochim Cosmochim Acta, 70(6): 1439–1456

Ghosh S, Sarkar S (2010). Geochemistry of Permo-Triassic mudstone of the Satpura Gondwana basin, central India: clues for provenance. Chem Geol, 277(1−2): 78–100

Girty G H, Hanson A D, Yoshinobu A S, Knaack C, Johnson D (1993). Provenance of Paleozoic mudstones in a contact metamorphic aureole determined by rare earth element, Th, and Sc analyses, Sierra Nevada, California. Geology, 21(4): 363–366

Gu X X, Liu J M, Zheng M H, Tang J X, Qi L (2002). Provenance and tectonic setting of the Proterozoic turbidites in Hunan, south China: geochemical evidence. J Sediment Res, 72(3): 393–407

Han X, Dai J G, Lin J, Xu S, Liu B, Hu T, Zhang C, Wang C S (2022). An Oligocene-Miocene intermontane narrow lowland in the central Xizang Plateau: insights from provenance analysis and palynological record of a Cenozoic sedimentary succession. J Asian Earth Sci, 240: 105438

Han Z P, Sinclair H D, Li Y L, Wang C S, Tao Z, Qian X Y, Ning Z J, Zhang J W, Wen Y X, Lin J, Zhang B S, Xu M, Dai J, Zhou A, Liang H, Cao S (2019). Internal drainage has sustained low‐relief Xizang landscapes since the early Miocene. Geophys Res Lett, 46(15): 8741–8752

Hayashi K I, Fujisawa H, Holland H D, Ohmoto H (1997). Geochemistry of ~1.9 Ga sedimentary rocks from northeastern Labrador, Canada. Geochim Cosmochim Acta, 61(19): 4115–4137

He H Y, Sun J M, Li Q L, Zhu R X (2012). New age determination of the Cenozoic Lunpola basin, central Xizang. Geol Mag, 149(1): 141–145

Hu P Y, Zhai Q G, Jahn B M, Wang J, Li C, Chung S L, Lee H Y, Tang S H (2017). Late Early Cretaceous magmatic rocks (118–113 Ma) in the middle segment of the Bangong–Nujiang suture zone, Xizang Plateau: evidence of lithospheric delamination. Gondwana Res, 44: 116–138

Hu Z, Zhang W, Liu Y, Gao S, Li M, Zong K, Chen H, Hu S (2015). "Wave" signal-smoothing and mercury-removing device for laser ablation quadrupole and multiple collector ICPMS analysis: application to lead isotope analysis. Anal Chem, 87(2): 1152–1157

Ingalls M, Rowley D B, Currie B S, Colman A S (2020). Reconsidering the uplift history and peneplanation of the northern Lhasa terrane, Xizang. Am J Sci, 320(6): 479–532

Jia G D, Bai Y, Ma Y J, Sun J M, Peng P A (2015). Paleoelevation of Xizang Lunpola basin in the Oligocene-Miocene transition estimated from leaf wax lipid dual isotopes. Global Planet Change, 126: 14–22

Jia J L, Liu Z J, Bechtel A, Strobl S A, Sun P C (2013). Tectonic and climate control of oil shale deposition in the Upper Cretaceous Qingshankou Formation (Songliao Basin, NE China). Int J Earth Sci, 102(6): 1717–1734

Jia L B, Su T, Huang Y J, Wu F X, Deng T, Zhou Z K (2019). First fossil record of *Cedrelospermum* (Ulmaceae) from the Qinghai-Xizang Plateau: implications for morphological evolution and biogeography. J Syst Evol, 57(2): 94–104

Jiang H, Su T, Wong W O, Wu F X, Huang J, Shi G (2019). Oligocene *Koelreuteria* (Sapindaceae) from the Lunpola Basin in central Xizang and its implication for early diversification of the genus. J Asian Earth Sci, 175: 99–108

Jones B, Manning D A (1994). Comparison of geochemical indices

used for the interpretation of palaeoredox conditions in ancient mudstones. Chem Geol, 111(1−4): 111–129

Kapp P, DeCelles P G (2019). Mesozoic-Cenozoic geological evolution of the Himalayan-Xizang orogen and working tectonic hypotheses. Am J Sci, 319(3): 159–254

Kapp P, DeCelles P G, Gehrels G E, Heizler M, Ding L (2007). Geological records of the Lhasa-Qiangtang and Indo-Asian collisions in the Nima area of central Xizang. Geol Soc Am Bull, 119(7−8): 917–933

Kasanzu C, Maboko M A, Manya S (2008). Geochemistry of fine-grained clastic sedimentary rocks of the Neoproterozoic Ikorongo Group, NE Tanzania: implications for provenance and source rock weathering. Precambrian Res, 164(3−4): 201–213

Kirubakaran N, Sridharan M, Senthil Nathan D, Rajamanickam M, Harikrishnan S (2023). Geochemical and sedimentological signatures of Ariyankuppam and Chunnambar Estuarine Sediments, Pondicherry, India: implications on weathering and provenance. J Geol Soc India, 99(9): 1275–1284

Kong X, Mi W T, Zhu L D, Yang W G (2019). Zircon U-Pb chronology and provenance of the Paleogene sandstones in the Nima Basin, Xizang: implication for coeval paleogeography. Arab J Geosci, 12: 1–17

Lee H Y, Chung S L, Ji J, Qian Q, Gallet S, Lo C H, Lee T Y, Zhang Q (2012). Geochemical and Sr-Nd isotopic constraints on the genesis of the Cenozoic Linzizong volcanic successions, southern Xizang. J Asian Earth Sci, 53: 96–114

Lerman A (1989). Lakes Chemistry and Geology Physics. Texas: Geological Press

Lézin C, Andreu B, Pellenard P, Bouchez J L, Emmanuel L, Fauré P, Landrein P (2013). Geochemical disturbance and paleoenvironmental changes during the Early Toarcian in NW Europe. Chem Geol, 341: 1–15

Li C, Zhao Z B, Lu H J, Li H B (2022c). Late Mesozoic-Cenozoic multistage exhumation of the central Bangong-Nujiang suture, central Xizang. Tectonophysics, 827: 229268

Li L, Lu H J, Garzione C, Fan M J (2022b). Cenozoic paleoelevation history of the Lunpola Basin in Central Xizang: new evidence from volcanic glass hydrogen isotopes and a critical review. Earth Sci Rev, 231: 104068

Li X L, Zhang X, Lin C M, Huang S Y, Li X (2022a). Overview of the application and prospect of common chemical weathering indices. Geol J China U, 28(1): 51

Li Y L, He J, Han Z P, Wang C S, Ma P F, Zhou A, Liu S A, Xu M (2016). Late Jurassic sodium-rich adakitic intrusive rocks in the southern Qiangtang terrane, central Xizang, and their implications for the Bangong–Nujiang Ocean subduction. Lithos, 245: 34–46

Li Y L, He J, Wang C S, Santosh M, Dai J G, Zhang Y X, Wei Y S, Wang J G (2013). Late Cretaceous K-rich magmatism in central Xizang: evidence for early elevation of the Xizang plateau. Lithos, 160–161: 1–3

Li Y L, Wang C S, Dai J G, Xu G Q, Hou Y L, Li X H (2015). Propagation of the deformation and growth of the Xizang-Himalayan orogen: a review. Earth Sci Rev, 143: 36–61

Liang J L, Tang D Z, Xu H, Tao S, Li C C, Gou M F (2014). Formation conditions of Jimusaer oil shale at the northern foot of Bogda Mountain, China. Oil Shale, 31(1): 19

Lin C M, Zhang X, Zhao X P, Li X, Huang S Y, Jiang K X (2021). Review of laboratory research methods for sedimentary petrology. Journal of Palaeogeography (Chinese Ed), 23(2): 223–244 (in Chinese)

Lin J, Liu Y, Yang Y, Hu Z (2016). Calibration and correction of LA-ICP-MS and LA-MC-ICP-MS analyses for element contents and isotopic ratios. Solid Earth Sci, 1(1): 5–27

Liu D, Shi R, Ding L, Huang Q, Zhang X, Yue Y, Zhang L (2017). Zircon U–Pb age and Hf isotopic compositions of Mesozoic granitoids in southern Qiangtang, Xizang: implications for the subduction of the Bangong–Nujiang Tethyan Ocean. Gondwana Res, 41: 157–172

Liu J, Su T, Spicer R A, Tang H, Wu F X, Srivastava G, Spicer T, Van Do T, Deng T, Zhou Z K (2019). Biotic interchange through lowlands of Xizang Plateau suture zones during Paleogene. Palaeogeogr Palaeoclimatol Palaeoecol, 524: 33–40

Liu X, Gao R, Guo X, Ding L (2023). Detrital zircon U-Pb geochronology of the Lunpola basin strata constrains the Cenozoic tectonic evolution of central Xizang. Gondwana Res, 113: 179–193

Lu L, Jin X, Yan L, Li W, Wei T, Shen Y (2024). Early uplift and exhumation of the Tanggula granitoid pluton since the Late Cretaceous: implications for the stepwise topographic growth model in the eastern Qiangtang terrane. Geol Soc Am Bull, 147–148: 22

Ma P F, Wang L C, Wang C S, Wu X H, Wei Y S (2015). Organic-matter accumulation of the lacustrine Lunpola oil shale, central Xizang Plateau: controlled by the paleoclimate, provenance, and drainage system. Int J Coal Geol, 147: 58–70

Madhavaraju J (2015). Geochemistry of late Cretaceous sedimentary rocks of the Cauvery Basin, south India: constraints on paleoweathering, provenance, and end Cretaceous environments. In: Ramkumar M, ed. Chemostratigraphy. Netherlands: Elsevier Science, 185–214

Madukwe H Y, Ayodele S O, Akinyemi S A, Adebayo O F (2016). Classification, maturity, provenance, tectonic setting, and source-area weathering of Ipole and Erin Ijesa stream sediments, south west Nigeria. Intern J Adv Sci Techn Res, 6(1): 232–255

Mao Z Q, Meng Q Q, Fang X M, Zhang T, Wu F L, Yang Y, Zhang W L, Zan J B, Tan M Q (2019). Recognition of tuffs in the middle-upper Dingqinghu Fm., Lunpola Basin, central Xizang Plateau: constraints on stratigraphic age and implications for paleoclimate. Palaeogeogr Palaeoclimatol Palaeoecol, 525: 44–56

McLennan S M, Hemming S R, Taylor S R, Eriksson K A (1995). Early Proterozoic crustal evolution: geochemical and Nd-Pb isotopic evidence from metasedimentary rocks, southwestern North America. Geochim Cosmochim Acta, 59(6): 1153–1177

McLennan S M, Hemming S, McDaniel D K, Hanson G N (1993). Geochemical approaches to sedimentation, provenance, and tectonics. Special Papers-Geological Society of America, 21–21

McLennan S M, Taylor S R, Eriksson K A (1983). Geochemistry of Archean shales from the Pilbara Supergroup, western Australia. Geochim Cosmochim Acta, 47(7): 1211–1222

McLennan S M, Taylor S R, Hemming S R (2006). Composition, Differentiation, and Evolution of Continental Crust: Constraints from Sedimentary Rocks and Heat Flow. Cambridge, UK:

Cambridge University Press

Meng Q T, Liu Z J, Bruch A A, Liu R, Hu F (2012). Palaeoclimatic evolution during Eocene and its influence on oil shale mineralisation, Fushun basin, China. J Asian Earth Sci, 45: 95–105

Mi W T, Yang W G, Zhu L D, Wu C G, Chen A Q (2018). Provenance of paleogene sediments in the south depression of Nima Basin, central Xizang and its geological implications. Geotectonica et Metallogenia, 42(1): 16 (in Chinese)

Michalopoulos P, Aller R C (1995). Rapid clay mineral formation in Amazon delta sediments: reverse weathering and oceanic elemental cycles. Science, 270(5236): 614–617

Molnar P, Boos W R, Battisti D S (2010). Orographic controls on climate and paleoclimate of Asia: thermal and mechanical roles for the Xizang Plateau. Annu Rev Earth Planet Sci, 38(1): 77–102

Molnar P, England P, Martinod J (1993). Mantle dynamics, uplift of the Xizang Plateau, and the Indian monsoon. Rev Geophys, 31(4): 357–396

Moradi A V, Sarı A, Akkaya P (2016). Geochemistry of the Miocene oil shale (Hançili Formation) in the Çankırı-Çorum Basin, Central Turkey: implications for paleoclimate conditions, source–area weathering, provenance and tectonic setting. Sediment Geol, 341: 289–303

Nesbitt H W (1979). Mobility and fractionation of rare earth elements during weathering of a granodiorite. Nature, 279(5710): 206–210

Nesbitt H W, Markovics G (1997). Weathering of granodioritic crust, long-term storage of elements in weathering profiles, and petrogenesis of siliciclastic sediments. Geochim Cosmochim Acta, 61(8): 1653–1670

Nesbitt H, Young G M (1982). Early Proterozoic climates and plate motions inferred from major element chemistry of lutites. Nature, 299(5885): 715–717

Potter P E (1978). Petrology and chemistry of modern big river sands. J Geol, 86(4): 423–449

Qiu X W, Liu C Y, Wang F F, Deng Y, Mao G Z (2015). Trace and rare earth element geochemistry of the Upper Triassic mudstones in the southern Ordos Basin, central China. Geol J, 50(4): 399–413

Ramos-Vázquez M A, Armstrong-Altrin J S (2019). Sediment chemistry and detrital zircon record in the Bosque and Paseo del Mar coastal areas from the southwestern Gulf of Mexico. Mar Pet Geol, 110: 650–675

Rasmussen C, Brantley S, Richter D D, Blum A, Dixon J, White A F (2011). Strong climate and tectonic control on plagioclase weathering in granitic terrain. Earth Planet Sci Lett, 301(3−4): 521–530

Raymo M E, Ruddiman W F (1992). Tectonic forcing of late Cenozoic climate. Nature, 359(6391): 117–122

Roddaz M, Viers J, Brusset S, Baby P, Boucayrand C, Hérail G (2006). Controls on weathering and provenance in the Amazonian foreland basin: insights from major and trace element geochemistry of Neogene Amazonian sediments. Chem Geol, 226(1−2): 31–65

Rohrmann A, Kapp P, Carrapa B, Reiners P W, Guynn J, Ding L, Heizler M (2012). Thermochronologic evidence for plateau formation in central Xizang by 45 Ma. Geology, 40(2): 187–190

Roser B P, Cooper R A, Nathan S, Tulloch A J (1996). Reconnaissance sandstone geochemistry, provenance, and tectonic setting of the lower Paleozoic terranes of the West Coast and Nelson, New Zealand. N Z J Geol Geophys, 39(1): 1–16

Roser B P, Korsch R J (1988). Provenance signatures of sandstone-mudstone suites determined using discriminant function analysis of major-element data. Chem Geol, 67(1−2): 119–139

Ross D J, Bustin R M (2009). Investigating the use of sedimentary geochemical proxies for paleoenvironment interpretation of thermally mature organic-rich strata: examples from the Devonian-Mississippian shales, Western Canadian Sedimentary Basin. Chem Geol, 260(1−2): 1–19

Rowley D B, Currie B S (2006). Palaeo-altimetry of the late Eocene to Miocene Lunpola Basin, central Xizang. Nature, 439(7077): 677–681

Rowley D B, Ingalls M, Colman A S, Currie B, Li S, Olack G, Lin D (2015). ~55 Ma aged high topography of the Lhasa Block From Stable and clumped isotope paleoaltimetry: implications for ~50±25% crustal mass deficit in the India-Asia collisional system. In AGU Fall Meeting Abstracts, Vol. 2015, T12B–06

Roy P D, Caballero M, Lozano R, Smykatz-Kloss W (2008). Geochemistry of late quaternary sediments from Tecocomulco lake, central Mexico: implication to chemical weathering and provenance. Chem Erde, 68(4): 383–393

Shekhar S, Shukla A, Kumar P (2018). Geochemical and petrographic interpretation of Sandhan Formation: an insight into provenance, tectonics and paleoclimatic conditions. Earth Sci India, 11(3): 11

Singh P (2009). Major, trace and REE geochemistry of the Ganga River sediments: influence of provenance and sedimentary processes. Chem Geol, 266(3−4): 242–255

Snell K E, Thrasher B L, Eiler J M, Koch P L, Sloan L C, Tabor N J (2013). Hot summers in the Bighorn Basin during the early Paleogene. Geology, 41(1): 55–58

Spicer R A, Su T, Valdes P J, Farnsworth A, Wu F X, Shi G, Spicer T E, Zhou Z (2021b). The topographic evolution of the Xizang Region as revealed by palaeontology. Palaeobiodivers Palaeoenviron, 101(1): 213–243

Spicer R A, Su T, Valdes P J, Farnsworth A, Wu F X, Shi G, Spicer T E, Zhou Z (2021a). Why 'the uplift of the Xizang Plateau' is a myth. Nat Sci Rev, 8(1): 091

Su T, Farnsworth A, Spicer R A, Huang J, Wu F X, Liu J, Li S F, Xing Y W, Huang Y J, Deng W Y D, Tang H, Xu C L, Zhao F, Srivastava G, Valdes P J, Deng T, Zhou Z K (2019). No high Xizang Plateau until the Neogene. Sci Adv, 5(3): eaav2189

Su T, Spicer R A, Wu F X, Farnsworth A, Huang J, Del Rio C, Deng T, Ding L, Deng W Y D, Huang Y J, Hughes A, Jia L B, Jin J H, Li S F, Liang S Q, Liu J, Liu X Y, Sherlock S, Spicer T, Srivastava G, Tang H, Valdes P, Wang T X, Widdowson M, Wu M X, Xing Y W, Xu C L, Yang J, Zhang C, Zhang S T, Zhang X W, Zhao F, Zhou Z K (2020). A Middle Eocene lowland humid subtropical "Shangri-La" ecosystem in central Xizang. Proc Natl Acad Sci USA, 117(52): 32989–32995

Sun J M, Xu Q H, Liu W M, Zhang Z Q, Xue L, Zhao P (2014). Palynological evidence for the latest Oligocene−early Miocene paleoelevation estimate in the Lunpola Basin, central Xizang. Palaeogeogr Palaeoclimatol Palaeoecol, 399: 21–30

Sun S, Chen A Q, Chen H D, Hou M C, Yang S, Xu S L, Wang F,

Huang Z F, Ogg J G (2022). Early Permian chemical weathering indices and paleoclimate transition linked to the end of the coal-forming episode, Ordos Basin, North China Craton. Palaeogeogr Palaeoclimatol Palaeoecol, 585: 110743

Tang H, Liu J, Wu F X, Spicer T, Spicer R A, Deng W Y D, Xu C L, Zhao F, Huang J, Li S F, Su T, Zhou Z K (2019). Extinct genus Lagokarpos reveals a biogeographic connection between Xizang and other regions in the Northern Hemisphere during the Paleogene. J Syst Evol, 57(6): 670–677

Taylor S R, McLennan S M (1985). The Continental Crust: Its Composition and Evolution. Oxford: Blackwell Scientific, 312

Tribovillard N, Algeo T J, Lyons T, Riboulleau A (2006). Trace metals as paleoredox and paleoproductivity proxies: an update. Chem Geol, 232(1−2): 12–32

Verma S P, Armstrong-Altrin J S (2013). New multi-dimensional diagrams for tectonic discrimination of siliciclastic sediments and their application to Precambrian basins. Chem Geol, 355: 117–133

Verma S P, Armstrong-Altrin J S (2016). Geochemical discrimination of siliciclastic sediments from active and passive margin settings. Sediment Geol, 332: 1–12

Vital H, Stattegger K (2000). Major and trace elements of stream sediments from the lowermost Amazon River. Chem Geol, 168(1−2): 151–168

Wang C S, Dai J G, Zhao X X, Li Y L, Graham S A, He D F, Ran B, Meng J (2014a). Outward-growth of the Xizang Plateau during the Cenozoic: a review. Tectonophysics, 621: 1–43

Wang H, Dutta S, Kelly R S, Rudra A, Li S, Zhang Q Q, Zhang Q Q, Wu Y X, Cao M Z, Wang B, Li J G, Zhang H C (2018b). Amber fossils reveal the Early Cenozoic dipterocarp rainforest in central Xizang. Palaeoworld (Amst), 27(4): 506–513

Wang P, Du Y, Yu W, Algeo T J, Zhou Q, Xu Y, Qi L, Yuan L, Pan W (2020). The chemical index of alteration (CIA) as a proxy for climate change during glacial-interglacial transitions in Earth history. Earth Sci Rev, 201: 103032

Wang Q, Zhu D C, Zhao Z D, Liu S A, Chung S L, Li S M, Liu D, Dai J G, Wang L Q, Mo X X (2014b). Origin of the ca. 90 Ma magnesia-rich volcanic rocks in SE Nyima, central Xizang: products of lithospheric delamination beneath the Lhasa-Qiangtang collision zone. Lithos, 198–199: 24–37

Wang S F, Ch Y, Yi H S, Tang W Q, Zhou Y X, Cui R L, Wu X H, Bai R, Yang Y (2023). The characteristics of *n*-alkanes from the Palaeogene lacustrine oil shale in the Kanggale area, Nyima Basin, and their paleoenvironment and Paleoclimate significance. Sediment Geol Tethyan Geol, 43(3): 542–554

Wang Z W, Wang J, Fu X G, Feng X L, Wang D, Song C Y, Chen W B, Zeng S Q (2017a). Petrography and geochemistry of upper Triassic sandstones from the Tumengela Formation in the Woruo Mountain area, North Qiangtang Basin, Xizang: implications for provenance, source area weathering, and tectonic setting. Isl Arc, 26(4): e12191

Wang Z W, Wang J, Fu X G, Zhan W Z, Armstrong-Altrin J S, Yu F, Feng X L, Song C Y, Zeng S Q (2018a). Geochemistry of the Upper Triassic black mudstones in the Qiangtang Basin, Xizang: implications for paleoenvironment, provenance, and tectonic setting. J Asian Earth Sci, 160: 118–135

Wang Z W, Wang J, Fu X G, Zhan W Z, Yu F, Feng X, Song C L, Chen W B, Zeng S Q (2017b). Organic material accumulation of Carnian mudstones in the North Qiangtang Depression, eastern Tethys: controlled by the paleoclimate, paleoenvironment, and provenance. Mar Pet Geol, 88: 440–457

Wei Y, Zhang K X, Garzione C N, Xu Y D, Song B W, Ji J L (2016). Low palaeoelevation of the northern Lhasa terrane during late Eocene: fossil foraminifera and stable isotope evidence from the Gerze Basin. Sci Rep, 6(1): 27508

Weltje G J, von Eynatten H (2004). Quantitative provenance analysis of sediments: review and outlook. Sediment Geol, 171(1−4): 1–11

Wesolowski D J (1992). Aluminum speciation and equilibria in aqueous solution: I. The solubility of gibbsite in the system Na-K-Cl-OH-Al $(OH)_4$ from 0 to 100 °C. Geochim Cosmochim Acta, 56(3): 1065–1091

West A J (2012). Thickness of the chemical weathering zone and implications for erosional and climatic drivers of weathering and for carbon-cycle feedbacks. Geology, 40(9): 811–814

Wronkiewicz D J, Condie K C (1987). Geochemistry of Archean shales from the Witwatersrand Supergroup, South Africa: source-area weathering and provenance. Geochim Cosmochim Acta, 51(9): 2401–2416

Wu F X, Miao D S, Chang M M, Shi G L, Wang N (2017). Fossil climbing perch and associated plant megafossils indicate a warm and wet central Xizang during the late Oligocene. Sci Rep, 7(1): 878

Xia G Q, Zheng D R, Krieg-Jacquier R, Fan Q S, Chen Y, Nel A (2022). The oldest-known Lestidae (Odonata) from the late Eocene of Xizang: palaeoclimatic implications. Geol Mag, 159(4): 511–518

Xiong Z Y, Liu X H, Ding L, Farnsworth A, Spicer R A, Xu Q, Valdes P, He S L, Zeng D, Wang C, Li Z Y, Guo X D, Su T, Zhao C Y, Wang H Q, Yue Y H (2022). The rise and demise of the Paleogene Central Xizang Valley. Sci Adv, 8(6): 0944

Xu X L, Shao L Y (2018). Limiting factors in utilization of chemical index of alteration of mudstones to quantify the degree of weathering in provenance. J Palaeogeogr (Chn Ed), 020(003): 515–522 (in Chinese)

Xu X T, Szwedo J, Huang D Y, Deng W Y D, Obroślak M, Wu F X, Su T (2022). A new genus of spittlebugs (hemiptera, cercopidae) from the eocene of central Xizang Plateau. Insects, 13(9): 770

Xue W W, Najman Y, Hu X M, Persano C, Stuart F M, Li W, Ma A L, Wang Y (2022). Late Cretaceous to Late Eocene exhumation in the Nima area, central Xizang: implications for development of low relief topography of the Xizang Plateau. Tectonics, 41(3): e2021TC006989

Yan H, Long X, Wang X C, Li J, Wang Q, Yuan C, Sun M (2016). Middle Jurassic MORB-type gabbro, high-Mg diorite, calc-alkaline diorite and granodiorite in the Ando area, central Xizang: evidence for a slab roll-back of the Bangong-Nujiang Ocean. Lithos, 264: 315–328

Yang J H, Cawood P A, Du Y S, Li W Q, Yan J X (2016). Reconstructing Early Permian tropical climates from chemical weathering indices. Geol Soc Am Bull, 128(5−6): 739–751

Yang Y B, Nie J S, Miao Y F, Wan S M, Jonell T N (2022). Xizang Plateau uplift and environmental impacts: new progress and

perspectives. Front in Earth Sci, 10: 1020354

Zeng S Q, Wang J, Chen W B, Fu X G, Feng X L, Song C Y, Wang D, Sun W (2020). Geochemical constraints on the provenance, paleoenvironment, and tectonic setting of late Triassic mudstones in the western Qiangtang Basin, Xizang. Lithosphere, 12(5): 631–648

Zhang X, Gélin U, Spicer R A, Wu F, Farnsworth A, Chen P, Del Rio C, Li S, Liu J, Huang J, Spicer T E, Tomlinson K W, Valdes P J, Xu X, Zhang S, Deng T, Zhou Z, Su T (2022). Rapid Eocene diversification of spiny plants in subtropical woodlands of central Xizang. Nat Commun, 13(1): 3787

Zhou L, Friis H, Poulsen M L K (2015). Geochemical evaluation of the late Paleocene and early Eocene shales in Siri Canyon, Danish-Norwegian Basin. Mar Pet Geol, 61: 111–122

Zhu D C, Wang Q, Cawood P A, Zhao Z D, Mo X X (2017). Raising the Gangdese mountains in southern Xizang. J Geophys Res Solid Earth, 122(1): 214–223

Zhu D C, Wang Q, Zhao Z D, Chung S L, Cawood P A, Niu Y L, Liu S A, Wu F Y, Mo X X (2015). Magmatic record of India-Asia collision. Sci Rep, 5(1): 14289

Zhu D C, Zhao Z D, Niu Y, Dilek Y, Hou Z Q, Mo X X (2013). The origin and pre-Cenozoic evolution of the Xizang Plateau. Gondwana Res, 23(4): 1429–1454